Supplementary Materials for

Electron Activity-Driven Lithium Nucleation within Solid Electrolyte Interphase

Yan Liu[1, 2]†, Anhao Zuo[3, 4]†, Zhe Huang[5], Cong Zhong[2], Suting Weng[2], Jiayi Zhang[2], Ruihe Xing[2], Zicen Deng[1], Xiong Xiao[1], Lujia Zhou[1], Zhenwei Zhu[1], Gaoping Cao[1], Li Wang[6], Yejing Li[2], Zhe Li[3, 4*], Hao Zhang[1*], Xuefeng Wang[2*]

Corresponding author: Xuefeng Wang, wxf@iphy.ac.cn; Hao Zhang, dr.h.zhang@hotmail.com; Zhe Li, zhe_li@tsinghua.edu.cn;

Materials and Methods

Supplementary Note 1: Evolution of SEI Transport Theory

The conceptual framework for the solid electrolyte interphase (SEI) has shifted from a static, 2D passivation layer to a dynamic, 3D heterogeneous system (**Table S1**). In the foundational Peled Model,(*1*) the SEI was idealized as a purely ionic conductor and an absolute electronic insulator, based on 1D analytical physical-modeling. For decades, computational efforts, largely dominated by Density Functional Theory (DFT) and Molecular Dynamics (MD), focused on identifying solvent-reduction pathways and molecular-level behavior,(*2*) but often lacked kinetic and transport physics. Shi et al. advanced the field by combining DFT with mesoscale diffusion equations,(*3*) proposing a two-layer/two-mechanism model where the dense inner layer limits Li^+ transport *via* a Knock-off mechanism, assuming a wide-bandgap insulator with voltage-dependent defect thermodynamics.

However, the persistent growth of SEI and the phenomenon of battery self-discharge necessitated a move toward higher systemic complexity. Feng et al. employed DFT and AIMD with analytical models for grain boundaries (GBs), demonstrating that even intrinsically insulating components like Li_2CO_3 or LiF can facilitate electronic leakage *via* GB defects, which exhibit reduced bandgaps and electron-trapping states.(*4*) This was further supported by Perez-Beltran et al.,(*5*) who used first-principles kMC and DFT/AIMD to identify GBs as faster pathways for Li^+ transport and confirmed that favorable electronic transport acts as a trigger for cell failure.

Recent studies have solidified the necessity of considering electron-ion coupled kinetics. Xu et al., using hybrid AIMD/ReaxFF and DFT/Green's function methods, confirmed that SEI exhibits semiconductor-like electronic conductivity, which governs growth and "dead Li" formation.(*6*) Yao et al. introduced a classical nucleation model to quantify 2D *vs*. 3D growth modes, showing that high overpotential promotes ideal 2D growth by limiting electron tunneling.(*7*) Krauss et al. developed a diffusion-reaction transmission-line model demonstrating that diffusive electron transport governs long-term electrolyte reduction.(*8*) An et al., using DPMD and DFT, simulated Li cluster nucleation within a nanoscale amorphous SEI layer, identifying its nearly zero-bandgap as the channel for electron transport that triggers internal Li reduction.(*9*) Zhang et al. employed an atomically-informed phase-field model to reveal that electron tunneling dictates the self-limiting thickness of SEI and drives the sequential formation of its bilayer structure.(*10*)

In conclusion, the evolution of SEI transport theory indicates that increasing computational dimensionality and systemic integration are inevitable. Transitioning from a diffusion-limited to an electron-transfer-limited kinetic framework is essential for accurately predicting the nucleation, growth, and eventual failure of the SEI in next-generation high-energy batteries. This evolution has progressively highlighted the risk of internal lithium plating within the SEI. Early models assumed SEI to be an absolute electronic barrier; however, recent theoretical studies reveal that electronic leakage through grain boundaries, amorphous regions, and nearly zero-bandgap nanoscale layers creates localized reductive environments.(*4, 6, 9*) Under high-rate charging conditions, the mismatch between ionic flux and localized electronic conduction may trigger Li^+ reduction before it reaches the electrode surface. This interspatial plating can only be captured by electron-ion coupled kinetic models that account for the electronic states of the interphase.

Table S1. Evolution of SEI transport theory.

Representative Literature	Computational Evolution	Dimension	Electronic properties of SEI	Key points
Peled (1979)(*1*)	Analytical physical modeling	1D	Ideal insulator assumption	Established the SEI as a purely ionic-conducting/electronic-insulating layer.
Tasaki (2005)(*2*)	DFT + MD	0D (Molecules) 3D (Bulk & Interface)	Ignored	Focused on solvent reduction pathways; lacked kinetic & transport physics.
Shi et al. (2012)(*3*)	DFT + Mesoscale diffusion equations	3D lattice (atomistic) + 1D two-layer model (mesoscale)	Wide bandgap insulator & Voltage-dependent defect thermodynamics	Proposed two-layer/two-mechanism model; identified dense inorganic layer as the rate-limiting step, where interstitial Li^+ diffuses via Knock-off mechanism to maintain high O-coordination
Feng et al. (2021)(*4*)	DFT + AIMD + Analytical model for grain boundary (GB)	2D (GBs) & 3D (amorphous regions)	Reduced bandgaps & electron trapping states at GBs	Proved that electronic leakage occurs via GBs even in insulating components.
Yao et al. (2023)(*7*)	Classical Nucleation Model	2D vs. 3D nucleation and growth modes	Electron-tunneling barrier limits 3D growth	Quantified 2D/3D models; proved high overpotential (large current pulses) promotes ideal 2D growth.
Xu et al. (2023)(*6*)	Hybrid AIMD/ReaxFF + DFT/Green's Function	Spatial variance across thickness	Voltage-dependent differential conductance (Semiconductor-like)	Experimentally confirmed SEI as a semiconductor; growth is electron-leakage limited, which causes “dead Li” formation; O:S ratio determines this leakage.
Perez-Beltran et al. (2024)(*5*)	First-Principles KMC + DFT/AIMD	3D heterogeneous matrix & GBs	Electronic transport as a failure trigger	Identified grain boundaries as faster pathways for Li+ transport; Confirmed favorable electronic transport acts as the trigger for cell failure

Krauss et al. (2025)(*8*)	Diffusion-reaction transmission-line model	1D inner dense SEI layer	Diffusive electron transport	Demonstrated that diffusive electron transport governs long-term electrolyte reduction
An et al. (2025)(*9*)	DPMD + DFT	Nanoscale amorphous SEI layer (~1 nm thickness) between Li and solid electrolyte	Electronic conduction due to nearly zero bandgap of nanoscale SEI layer	Simulated isolated Li cluster nucleation within the amorphous SEI layer; Identified the nearly zero bandgap of the SEI as the channel for electron transport; Confirmed that electronic conduction through the SEI triggers internal Li reduction
Zhang et al. (2025)(*10*)	Atomically-informed phase-field model	1D (including inner dense & outer porous)	Electron tunneling-limited growth	Demonstrated that electron tunneling dictates the self-limiting thickness of SEI; Revealed a transport-induced sequential formation of the bilayer SEI structure

Supplementary Note 2: Preparation of Single-Layer Graphite Electrode

Graphite material and PVDF were mixed at a mass ratio of 95:5. PVDF was pre-dissolved in NMP at a 5% mass ratio. The mixture was weighed into a glass vial at a solid-to-liquid ratio of 1:5 and blended in NMP. The resulting slurry was then stirred on a magnetic stirrer for 12 h. The slurry was subsequently doctor-blade coated onto the rough side of a copper foil current collector using a film coater. A doctor blade with a gap of 20 μm was used to further control the active material loading between 0.2~0.4 $mg \cdot cm^{-2}$. The coated electrode was placed in an oven at 60 ℃ until the surface was dry, then transferred to a vacuum oven at 120 ℃ for 12 h to remove the NMP solvent. The dried electrode sheet was punched into small circular discs with a diameter of 12 mm using a disc cutter. Finally, the discs were weighed and stored in a dry Petri dish for later use. This study utilized coin cells as the test platform; the battery assembly process is described below.

Assembly of coin cells: CR2032 (316 stainless steel) type coin cells were used as the test platform for half-cells. Modifications specific to the electrodes in each chapter are described in the experimental sections of the respective chapters. The prepared electrode discs, lithium metal foil discs (15.6 mm diameter, 0.2 mm thickness), and Celgard 2500 separator discs (19 mm diameter) were assembled in the following sequence: positive electrode shell, electrode disc, separator, lithium disc, spacer, spring washer, and negative electrode shell. Approximately 60 μL of electrolyte (1.0 M $LiPF_6$ in EC/DEC, 1:1 v/v) was added. The assembled coin cell was sealed using a coin cell crimper and left to rest for 10 h to ensure thorough wetting of the electrode micropores by the electrolyte. The cells were then ready for subsequent electrochemical testing.

Supplementary Note 3: Electrochemical Testing and Material Characterization

Electrochemical Performance Testing of Half-Cells: The electrochemical performance of the assembled Graphite|Li half-cells was systematically evaluated using a Land CT3001A multi-channel battery testing system within a precision temperature-controlled chamber maintained at 25 ± 0.5 °C. An initial formation cycle was first performed at a low current density of 5 $\mu A \cdot cm^{-2}$. This stage promotes the formation of a uniform SEI layer with moderate electrochemical kinetics and establishes a stable interface structure between the graphite anode and the electrolyte. Subsequently, a strategy employing differentiated current densities (5 $\mu A \cdot cm^{-2}$ and 50 $\mu A \cdot cm^{-2}$) was designed to induce lithium nucleation behavior under different conditions. At the low current density of 5 $\mu A \cdot cm^{-2}$, the lithium deposition process is slow and uniform, facilitating observation of the nucleation process under near-ideal conditions. In contrast, at the high current density of 50 $\mu A \cdot cm^{-2}$, accelerated electrochemical reaction kinetics and enhanced electromigration effects intensify localized inhomogeneities on the electrode surface.

Field emission scanning electron microscopy (FE-SEM, Quanta 650FEG) operated at 10 kV, coupled with energy-dispersive X-ray spectroscopy (EDS) mapping, was employed to observe the morphology of pristine graphite particles, the electrode sheet, and the surface morphology, structure, and elemental distribution of graphite after lithium plating. Electrochemical impedance spectroscopy (EIS) measurements were conducted using an electrochemical workstation (BioLogic SP-200 system). The test conditions were: AC voltage amplitude of 10 mV, over a wide frequency range from 1 MHz to 0.1 Hz. Analysis of the resulting Nyquist plots provided key electrochemical parameters such as the ohmic resistance, interfacial charge transfer resistance, and solid-state diffusion resistance within the battery, offering crucial insights for understanding the kinetics of interfacial reactions and mass transport processes.

A Thermo Scientific K-Alpha+ X-ray photoelectron spectrometer (XPS) was utilized for precise surface analysis of the SEI film on the graphite anode. The analysis employed a monochromated 150W Al Kα X-ray source. Combined with controlled depth profiling using an argon ion beam, this technique enabled the chemical composition analysis of the SEI film at different depths, providing molecular-level chemical information to understand the electrode interfacial reaction mechanisms and lithium nucleation behavior. A PHI nanoTOF II time-of-flight secondary ion mass

spectrometer (ToF-SIMS) was used for high-sensitivity analysis of sample surface composition and depth profiling. Data acquisition utilized a 30 keV Bi_3^{++} primary ion beam with a mass detection range of 2-1,850 u. Surface cleaning was performed using a 3 keV Ar^+ ion beam for sputtering over a 400 μm × 400 μm scan area. The sputtering rate, calibrated against SiO_2, was 7.74 nm/min to ensure the acquisition of accurate interfacial chemical information.

Cryogenic transmission electron microscopy (cryo-TEM) analysis was performed using a JEOL JEM-F200 microscope operating at 200 kV, with the sample stage maintained at -180 ℃. The specific sample preparation procedure was as follows: Within an inert atmosphere glove box, powder samples were carefully scraped off from the pre-solvent-cleaned and thoroughly dried graphite electrode surface using a scalpel. The collected sample particles were then uniformly dispersed and loaded onto ultrathin carbon-coated microgrids. The prepared microgrids were precisely mounted onto a dedicated Fischione 2550 cryogenic specimen holder. After mounting, the holder tip was fully retracted and sealed inside the holder body, which was then covered with a protective sleeve. A high-efficiency dry vacuum pump was connected to evacuate the holder for ten minutes, ensuring a high-purity transfer environment. Following evacuation, the protective sleeve was removed, and the cryo-holder was rapidly and precisely inserted into the microscope vacuum chamber. Strict adherence to the operational protocol-confirming the holder was fully inserted into the chamber before extending the tip-ensured an oxygen-free transfer pathway, effectively preventing sample oxidation or contamination from air exposure. Liquid nitrogen was then precisely filled into the dedicated Dewar of the cryo-holder. After approximately one hour for thermal equilibration, the temperature at the holder tip stabilized at -180 ℃. High-resolution images were acquired and comprehensively analyzed using the DigitalMicrograph (DM) software system developed by Gatan. This allowed for the precise characterization of graphite structure and its surface components. Inverse Fast Fourier Transform (iFFT) digital image processing techniques were applied to the original TEM images for optimization, significantly improving the signal-to-noise ratio and enhancing the visualization quality of microstructural details.

The ImageJ professional image analysis software was employed for quantitative characterization of the interfacial phase micro-morphology. This involved calculating the area percentage of each component region relative to the total region to accurately estimate the content distribution of inorganic components within the interfacial phase.

Concurrently, grain boundaries were marked and analyzed to obtain grain size distribution characteristics, providing reliable quantitative data for correlating the microstructure of the interfacial phase with its properties.

Supplementary Note 4. Multiphysics Modeling of Heterogeneous SEI

A two-dimensional multiphysics model was developed to simulate coupled transport and reaction processes in lithium-ion batteries with heterogeneous solid electrolyte interphase (SEI) structures. The computational domain (**Fig. S1**) comprises four distinct regions, including a solid graphite electrode, a heterogeneous SEI film, a separator, and a lithium metal counter electrode. The SEI is modeled as a composite layer consisting of a porous organic matrix with embedded inorganic particles. Representative geometries for organic-rich and inorganic-rich configurations are illustrated in **Fig. S1**. The SEI thickness was set to 15 nm with a width of 200 nm, where the lower boundary interfaces with the graphite electrode and the upper boundary contacts the separator.

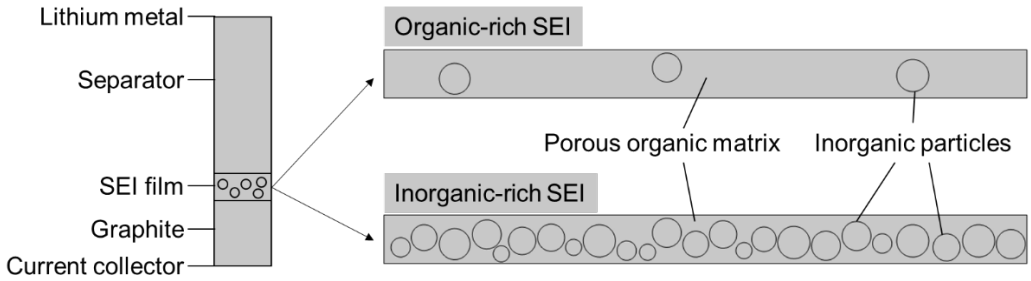

Fig. S1.
Simulation domains for the heterogeneous SEI model.

Lithium intercalation in the graphite electrode follows Fick's law of diffusion:

$$\frac{\partial c_s}{\partial t} = \nabla \cdot (D_s \nabla c_s) \tag{S1}$$

where c_s is the lithium concentration in the solid phase and D_s is the solid-state diffusion coefficient.

Electron transport through the graphite and the SEI is governed by Ohm's law:

$$i_s = -\sigma_s \nabla \phi_s \tag{S2}$$

where i_s is the electronic current density, σ_s is the electronic conductivity, and ϕ_s is the solid-phase potential.

The charge transfer reaction at the graphite/SEI interface is described by the Butler-Volmer (BV) equation:

$$i_{\mathrm{int}} = i_{0,\mathrm{int}}\left(e^{\frac{\alpha_{a,\mathrm{int}}F}{RT}\eta_{\mathrm{int}}} - e^{-\frac{\alpha_{c,\mathrm{int}}F}{RT}\eta_{\mathrm{int}}}\right) \quad \text{(S3)}$$

where $i_{0,\mathrm{int}}$ is the exchange current density for intercalation, $\alpha_{a,\mathrm{int}}$ and $\alpha_{c,\mathrm{int}}$ are the anodic and cathodic transfer coefficients, and η_{int} is the overpotential defined as $\eta_{\mathrm{int}} = \phi_{\mathrm{s}} - \phi_{\mathrm{l}} - U_{\mathrm{eq}}$, with U_{eq} being the equilibrium potential for graphite.

The lithium metal electrode is treated as a planar current collector, and the interfacial reaction is described by the BV equation:

$$i_{\mathrm{Li}} = i_{0,\mathrm{Li}}\left(e^{\frac{\alpha_{\mathrm{Li}}F}{RT}\eta_{\mathrm{Li}}} - e^{-\frac{(1-\alpha_{\mathrm{Li}})F}{RT}\eta_{\mathrm{Li}}}\right) \quad \text{(S4)}$$

$$\eta_{\mathrm{Li}} = -\phi_{\mathrm{l}} \quad \text{(S5)}$$

Here, i_{Li} and $i_{0,\mathrm{Li}}$ are the current density and exchange current density at the Li metal/electrolyte interface, respectively, and η_{Li} is the overpotential.

The model incorporates the possibility of metallic lithium deposition (plating) within the SEI bulk. The plating current density i_{pl} is governed by the BV equation, activated only when the local plating overpotential η_{pl} is negative:

$$i_{\mathrm{pl}} = i_{0,\mathrm{pl}}\left(e^{\frac{\alpha_{a,\mathrm{pl}}F}{RT}\eta_{\mathrm{pl}}} - e^{-\frac{\alpha_{c,\mathrm{pl}}F}{RT}\eta_{\mathrm{pl}}}\right) \quad \text{(S6)}$$

The exchange current density for plating $i_{0,\mathrm{pl}}$ is given by:

$$i_{0,\mathrm{pl}} = Fk_{\mathrm{pl}}\left(\frac{c_{\mathrm{Li^+}}}{c_{\mathrm{ref}}}\right)^{\alpha_{a,\mathrm{pl}}} \quad \text{(S7)}$$

where k_{pl} is the reaction rate constant for lithium plating, and c_{ref} is a reference concentration. The transfer coefficients are set to $\alpha_{a,\mathrm{pl}} = 0.3$ and $\alpha_{c,\mathrm{pl}} = 0.7$.(*11*) The overpotential for plating is defined as $\eta_{\mathrm{pl}} = \phi_{\mathrm{s}} - \phi_{\mathrm{l}} - U_{\mathrm{eq}}$, with the equilibrium potential U_{eq} for the Li^+/Li couple taken as 0 V vs. Li/Li^+.

Ion transport in the electrolyte (including the porous SEI and separator regions) is described by concentrated solution theory.(*12*) The electrolyte potential ϕ_{l} is governed by:

$$i_{\mathrm{l}} = -\kappa^{\mathrm{eff}}\nabla\phi_{\mathrm{l}} + \frac{2\kappa^{\mathrm{eff}}RT}{F}\left(1 + \frac{\partial \ln f_{\pm}}{\partial \ln c_{\mathrm{l}}}\right)(1 - t_+)\nabla \ln c_{\mathrm{l}} \quad \text{(S8)}$$

where i_{l} is the ionic current density, κ^{eff} is the effective ionic conductivity, t_+ is the Li^+ transference number, and c_{l} is the Li^+ concentration in the electrolyte.

The conservation of Li^+ in the electrolyte is given by:

$$\varepsilon \frac{\partial c_l}{\partial t} = \nabla \cdot \left(D_l^{eff} \nabla c_l\right) + (1 - t_+) \frac{\nabla \cdot i_l}{F} \quad \text{(S9)}$$

where ε is the porosity (volume fraction of the electrolyte phase), and D_l^{eff} is the effective diffusion coefficient in the electrolyte.

The Bruggeman relation is used to correlate the effective transport properties with the porosity of the porous media:

$$\kappa^{eff} = \varepsilon^{1.5} \kappa \quad \text{(S10)}$$

$$D_l^{eff} = \varepsilon^{1.5} D_l \quad \text{(S11)}$$

where κ and D_l are the bulk electrolyte properties. The organic SEI layer is modeled as a porous medium with 10% porosity, saturated with liquid electrolyte. Given that the ionic conductivity of the electrolyte (~0.73 S/m) is several orders of magnitude higher than that of the organic matrix,(*13*) Li^+ transport in the organic layer is dominated by the electrolyte phase. A parallel-conduction assumption is adopted to determine the effective ion conductivity in the composite organic domain.

The initial lithium ion concentration in the electrolyte is set to 1000 mol/m^3. The intrinsic ionic conductivities of the inorganic and organic SEI components are set to 1.0×10^{-7} S/m and 1.0×10^{-9} S/m, respectively.(*14*) The intrinsic electronic conductivities of the inorganic and organic SEI components are set to 1.0×10^{-9} S/m and 1.0×10^{-7} S/m, respectively. The corresponding Li^+ diffusion coefficients are estimated using the Einstein relation:(*15*)

$$D_{Li^+} = \frac{\sigma RT}{z^2 F^2 c_{Li^+}} \quad \text{(S12)}$$

where σ is the ionic conductivity of SEI components.

Electron transport through the insulating SEI components is modeled using quantum tunneling theory, which dominates over classical ohmic conduction in these regions. The steady-state Schrödinger equation is solved to obtain the electron wavefunction:

$$-\frac{\hbar^2}{2m^*} \nabla^2 \Psi(x,y) + V(x,y)\Psi(x,y) = 0 \quad \text{(S13)}$$

where $\Psi(x,y)$ is the electron wavefunction, $V(x,y)$ is the spatially dependent potential energy profile representing the SEI tunneling barrier, ħ is the reduced Planck constant, and m^* is the effective electron mass. The square modulus of the wavefunction, $|\Psi|^2$,

corresponds to the local electron probability density and is used to approximate the electron activity:(*16*)

$$a_{e^-}(x,y) = |\Psi(x,y)|^2 \quad \text{(S14)}$$

The electron activity provides a spatially resolved measure of electron availability for reduction reactions at any point within the SEI. This quantum-derived $a_{e^-}(x,y)$ is then coupled to the electrochemical reaction kinetics via Eq. (S6) in the main text, modifying the local exchange current density, rather than contributing to a classical continuum electron current i_s.

The electron tunneling barrier heights are set to 1.78 eV for the inorganic component, 0.24 eV for the organic component.(*16*) At the graphite surface (bottom boundary), the electron wavefunction is fixed as $\Psi = 1$ to represent electron-rich conditions. Zero-flux boundary conditions are applied for the wavefunction at the lateral boundaries, confining electron tunneling within the SEI without lateral leakage. These constraints enable the calculation of spatially resolved tunneling behavior.

The model was implemented in COMSOL Multiphysics. The model parameters are summarized in **Table S2**.

Table S2. Model parameters.

Parameter	Value	Source
Graphite thickness (μm)	5	Set
SEI thickness (nm)	15	Set
SEI width (nm)	200	Set
Separator thickness (μm)	10	Set
Organic SEI porosity (%)	10	Set
Inorganic phase ionic conductivity (S/m)	$1.0\text{x}10^{-7}$	Literature(*14*)
Organic phase ionic conductivity (S/m)	$1.0\text{x}10^{-9}$	Literature(*14*)
Inorganic phase electronic conductivity (S/m)	$1.0\text{x}10^{-9}$	Literature(*17*)
Organic phase electronic conductivity (S/m)	$1.0\text{x}10^{-7}$	Literature(*17*)
Inorganic phase tunneling barrier (eV)	1.78	Literature(*16*)
Organic phase tunneling barrier (eV)	0.24	Literature(*16*)

Li^+ conductivity in electrolyte (S/m)	0.73	Literature(*18*)
Li^+ diffusivity in electrolyte (m^2/s)	$1.0x10^{-10}$	Literature(*18*)
Li^+ transference number	0.38	Set
Initial Li^+ concentration in electrolyte (mol/m^3)	1000	Set
Plating reaction anodic transfer coefficient	0.3	Literature(*11*)
Plating reaction cathodic transfer coefficient	0.7	Literature(*11*)
Plating reaction rate constant ($mol/(m^2\ s)$)	$2.23x10^{-7}$	Literature(*11*)
Reference concentration (mol/m^3)	1	Set
Reaction rate constant for intercalation k (m/s)	$2.43x10^{-10}$	Literature(*18*)
Li^+ diffusion coefficient of graphite (m^2/s)	$1.45x10^{-13}$	Literature(*18*)
Exchange current density at Li/electrolyte interface (A/m^2)	100	Literature(*19*)

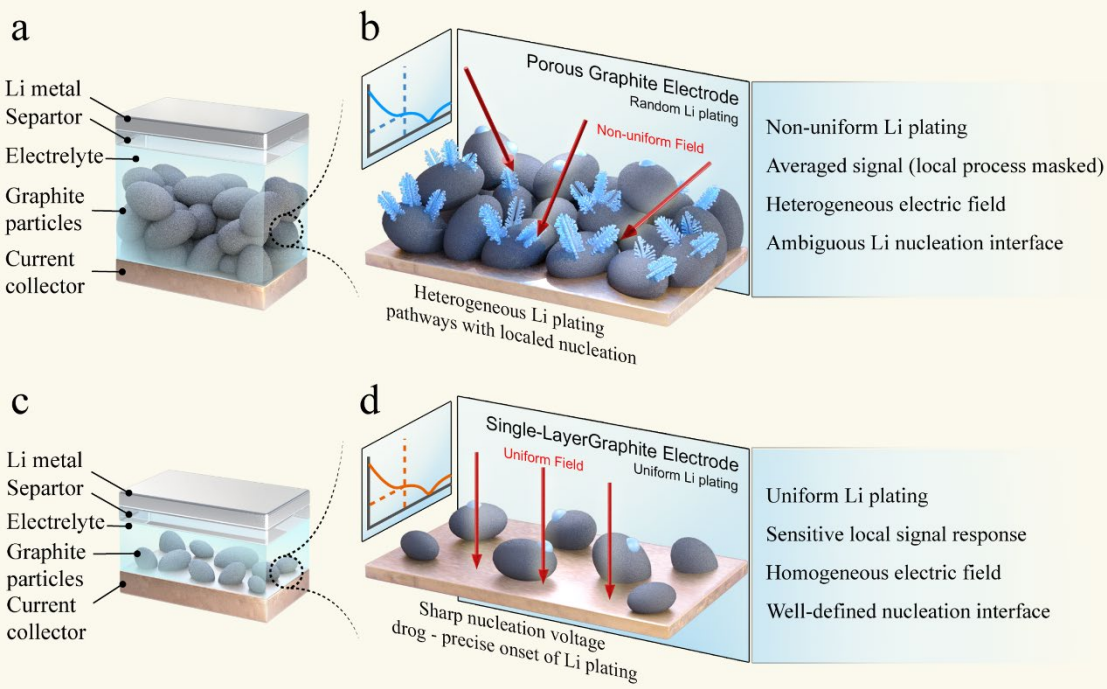

Fig. S2.

Design comparison of porous and monolayer graphite electrodes: (a) 3D and (b) 2D representations of porous electrode structure; (c) 3D and (d) 2D representations of monolayer electrode structure.

Precise nucleation threshold determination faces two fundamental challenges in porous electrodes (Fig. S2a, b). Spatially, random graphite particle stacking creates heterogeneous electric field distributions and divergent Li^+ diffusion pathways, causing temporally dispersed Li nuclei formation across different sites with inconsistent timing and size distributions. Electrochemically, the overwhelming Li intercalation currents from abundant graphite particles mask the subtle nucleation signatures. These combined effects manifest as gradual, featureless voltage-capacity transitions that obscure the precise moment of nucleation onset. The monolayer graphite electrode (MGE, **Fig. S2c, d**) addresses both challenges through spatiotemporal synchronization and signal amplification. The ordered arrangement eliminates spatial heterogeneity, ensuring temporally synchronized Li^+ reduction and simultaneous Li nuclei formation under uniform electrochemical environments. Simultaneously, the dramatically reduced graphite content amplifies nucleation signatures by minimizing competing intercalation signals, transforming previously imperceptible nucleation events into electrochemically distinguishable features.

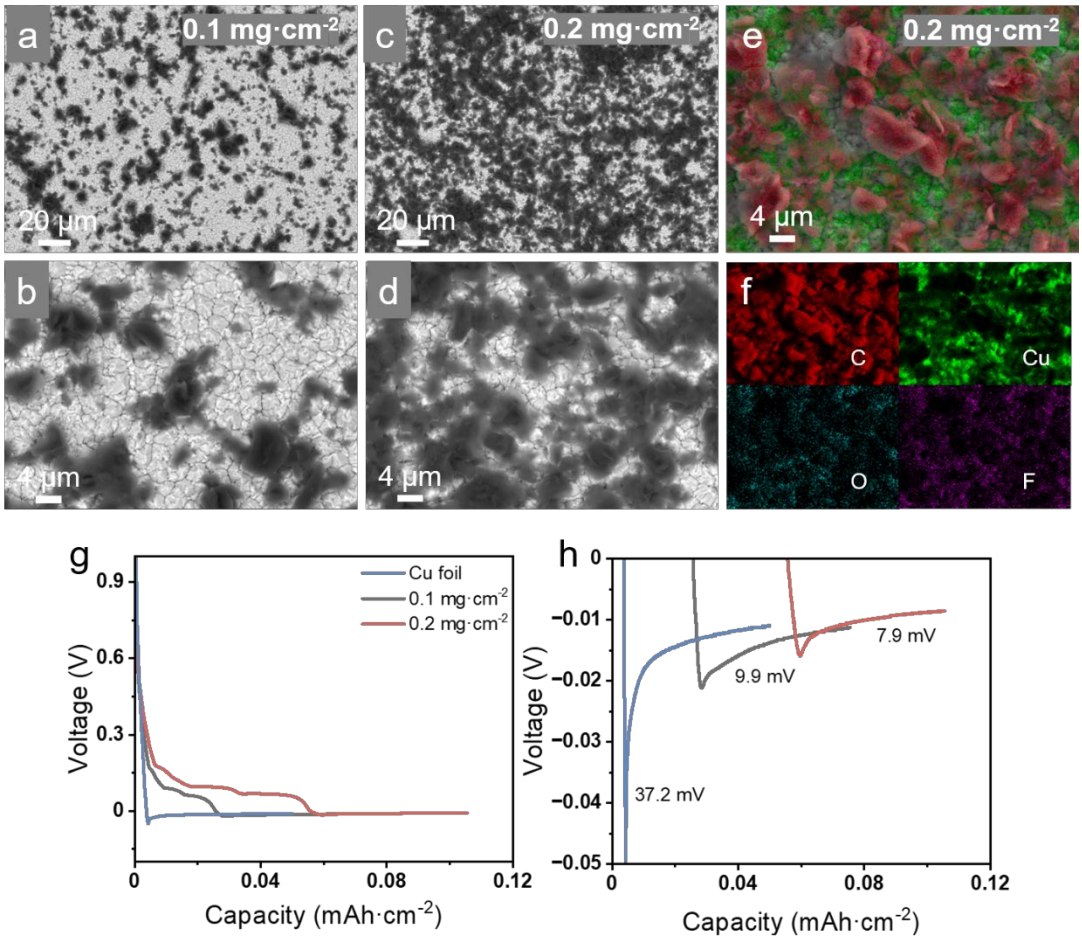

Fig. S3.

Morphological and compositional characterization of monolayer graphite electrodes. SEM images of graphite particle distribution at different mass loadings: (a-b) 0.1 mg·cm^{-2} and (c-d) 0.2 mg·cm^{-2}; (e) Energy Dispersive X-ray Spectroscopy (EDS) showing spatial distribution of graphite particles (red) and copper foil substrate (green); (f) Elemental mapping profiles revealing distribution characteristics of C, Cu, O, and F elements; (g) Voltage-capacity profiles of bare Cu foil and graphite electrodes with loadings of 0.1 and 0.2 mg cm^{-2} at a galvanostatic current density of 50 μA cm^{-2}; (h) Magnified view of the low-potential region (0 to −0.05 V). The intercalation capacity of the 0.2 mg cm^{-2} sample reaches approximately twice that of the 0.1 mg cm^{-2} sample, verifying the precise control of graphite loading during electrode fabrication.

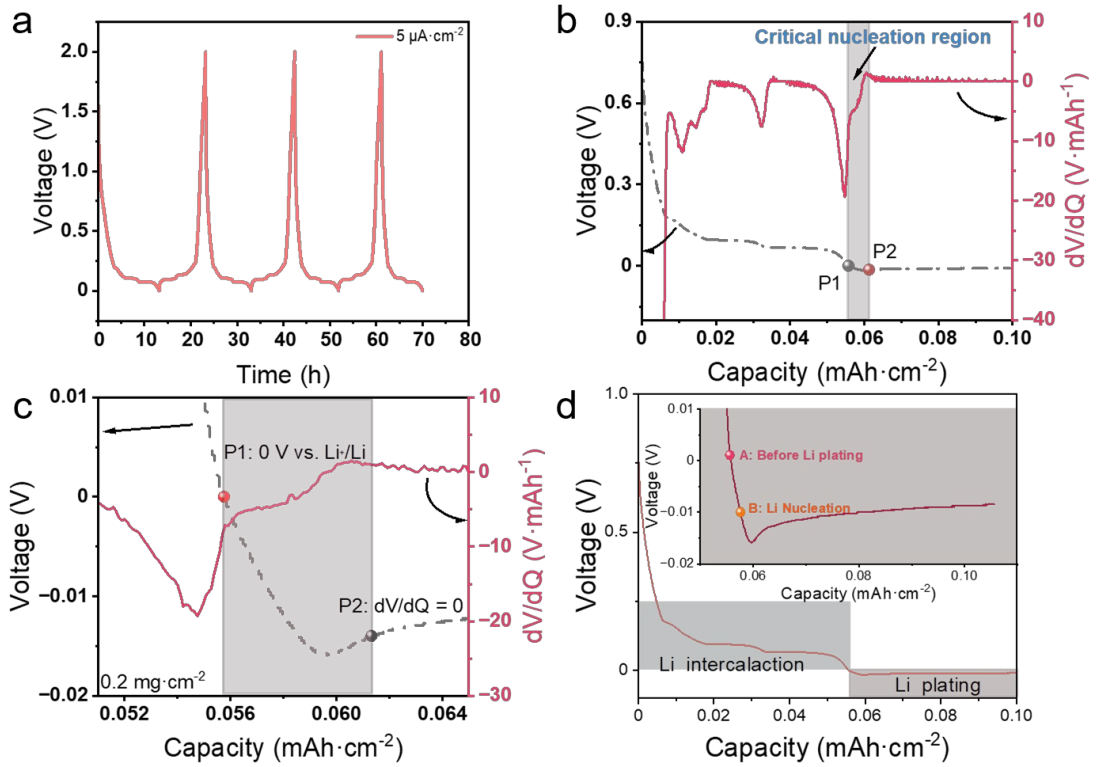

Fig. S4.

Electrochemical profiles and differential capacity analysis for lithium nucleation identification. (a) Voltage-time profiles during SEI formation at 5 μA cm^{-2}. (b) Voltage profile (black) and differential capacity curve (dV/dQ, red) during lithiation of MGE (0.2 mg cm^{-2} graphite loading). (c) Magnified view of the nucleation threshold region showing P1 (0 V vs. Li^+/Li) and P2 (dV/dQ ≈ 0) from 0 V to -14 mV vs. Li^+/Li; (d) Voltage-capacity profiles during lithium intercalation and nucleation; inset shows detailed electrochemical signatures below 0 V for nucleation state identification.

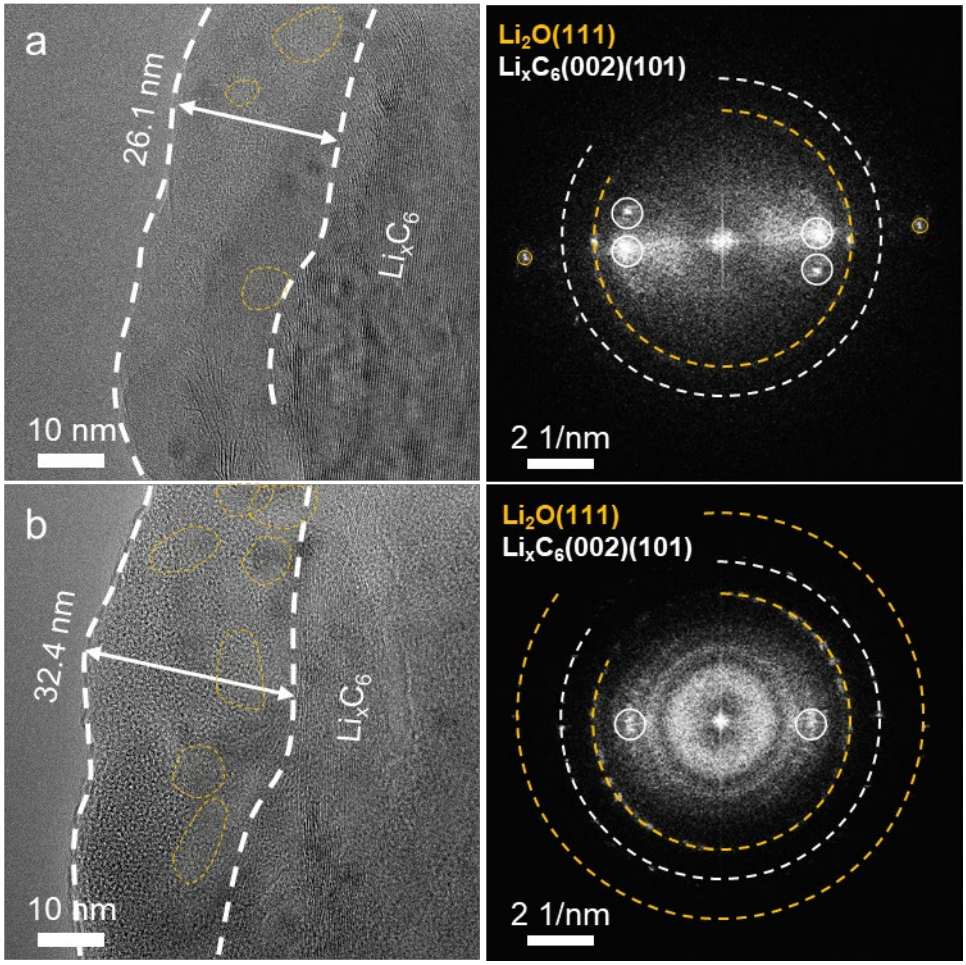

Fig. S5.

Structure and composition of the organic-rich SEI (5F-SEI). Cryo-TEM images and corresponding FFT patterns from two independent graphite particles are shown in (a) and (b), respectively.

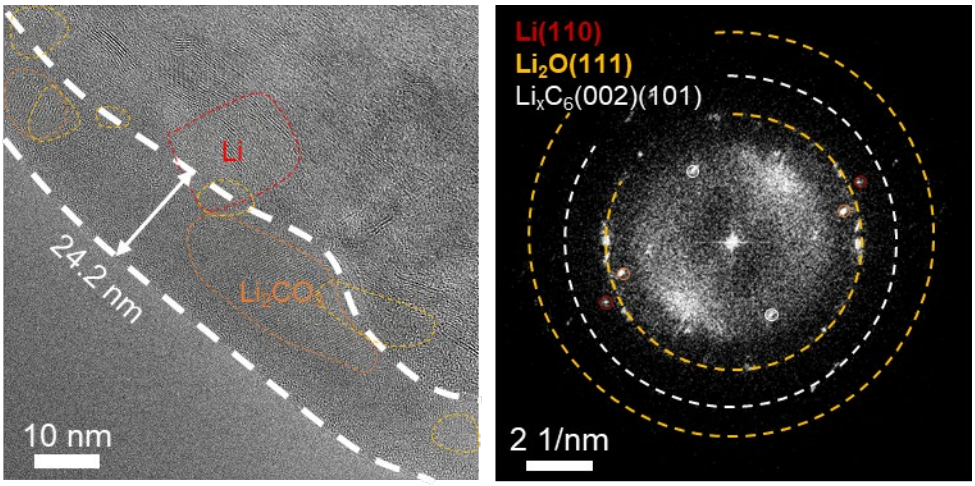

Fig. S6.

Cryo-TEM and FFT characterization of Li nucleation at the graphite surface.

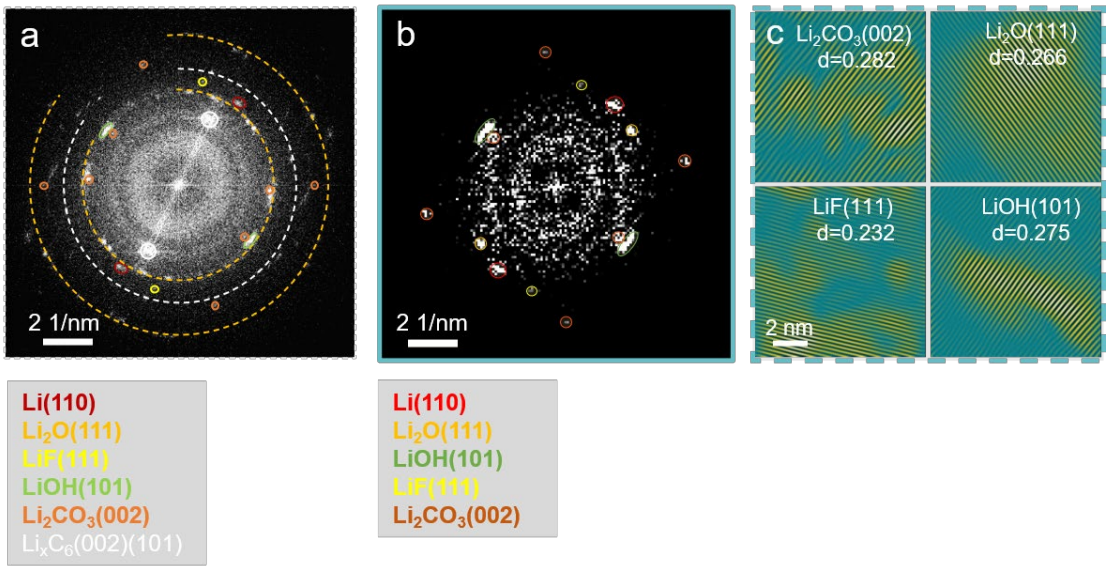

Fig. S7.

FFT patterns (a) from Fig. 1b and (b) from Fig. 1c. (c) Representative lattice structure for Li_2CO_3 ((002), 2.82 Å), LiOH ((101), 2.75 Å), Li_2O ((111), 2.66 Å), and LiF ((111), 2.32 Å).

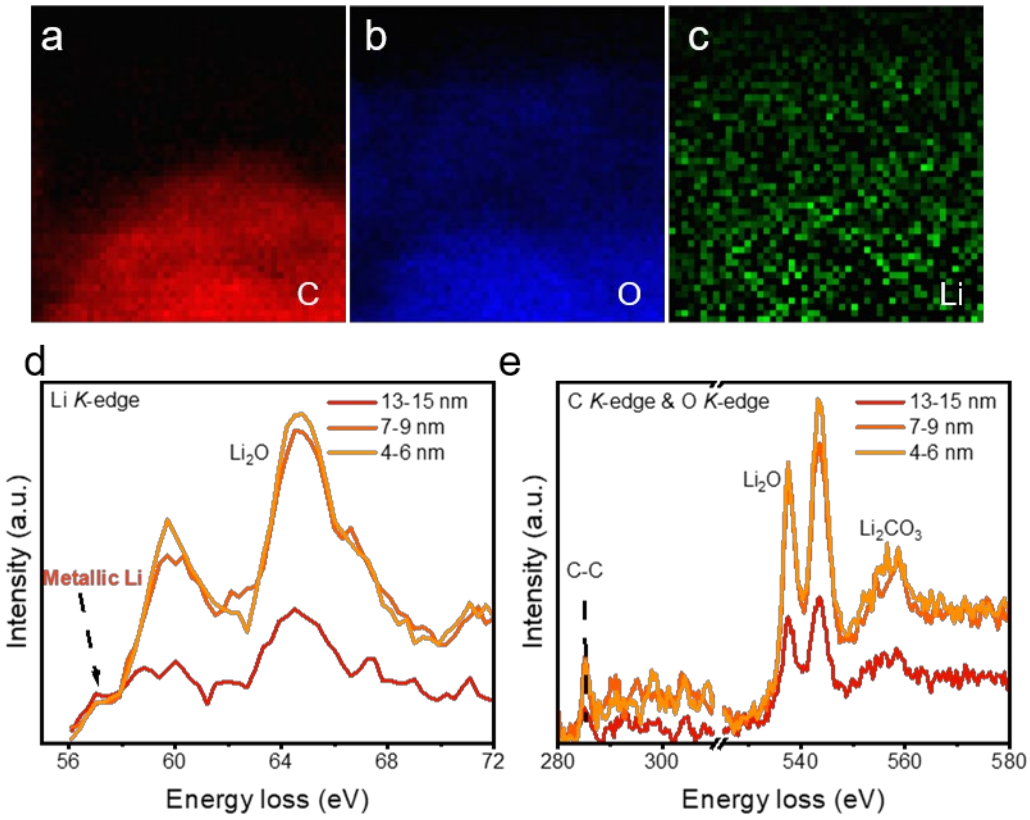

Fig. S8.

(a-c) EELS mapping images showing the carbon (C), oxygen (O), and lithium (Li); (d) Li *K*-edge and (e) C *K*-edge & O *K*-edge spectra extracted from depth-resolved regions at 4-6 nm, 10-12 nm, and 13-15 nm from the graphite surface.

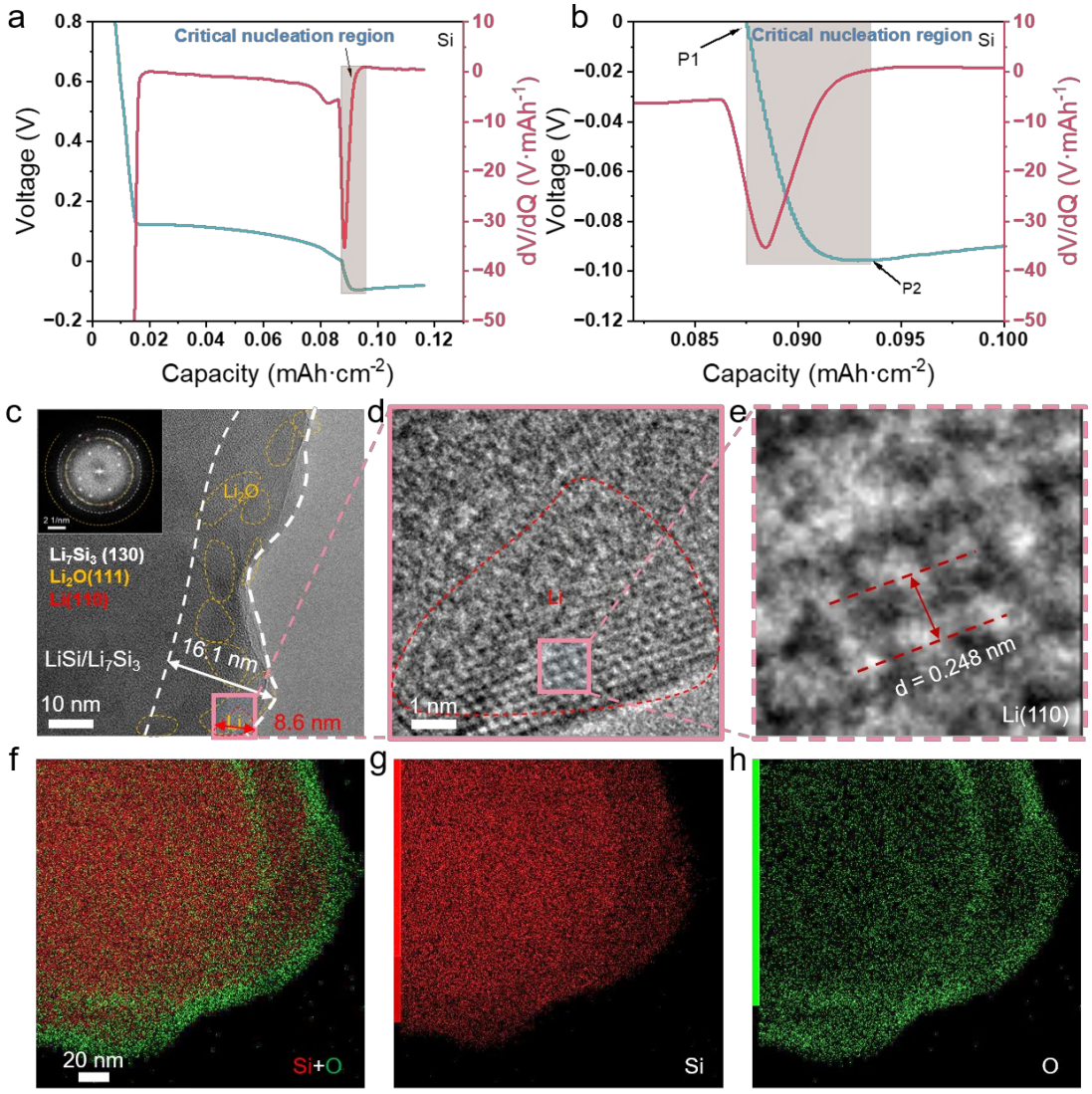

Fig. S9.

Differential capacity analysis (dV/dQ) of critical phase transition process on monolayer nano-Si platform: (a) Voltage-capacity curve of nano-Si electrode alloyed to 0 V under constant current of 5 μA·cm^{-2}, followed by Li nucleation at 50 μA·cm^{-2}; (b) Magnified view of the critical nucleation interval; (c) Cryo-TEM image of SEI on nano-Si anode; Inset: corresponding selected area electron diffraction (SAED) pattern; (d, e) High-resolution images of Li metal lattice from the pink boxed region in (c); EDS elemental mapping of nano-Si anode (f) overlapping Si+O, (g) Si, (h) O.

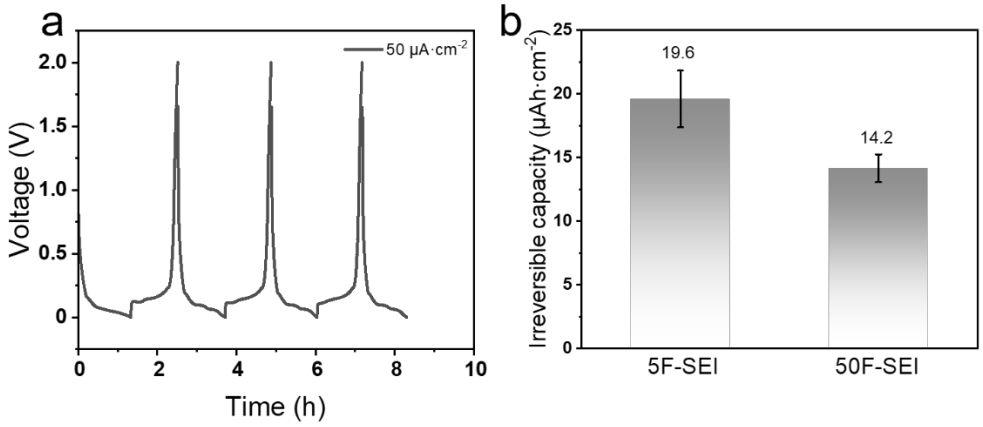

Fig. S10.

Voltage-time profiles during SEI formation on graphite anodes. (a) Electrochemical voltage profiles during galvanostatic lithiation at 50 μA cm^{-2} and (b) Comparison of irreversible capacities for 5 μA cm^{-2} and 50 μA cm^{-2}.

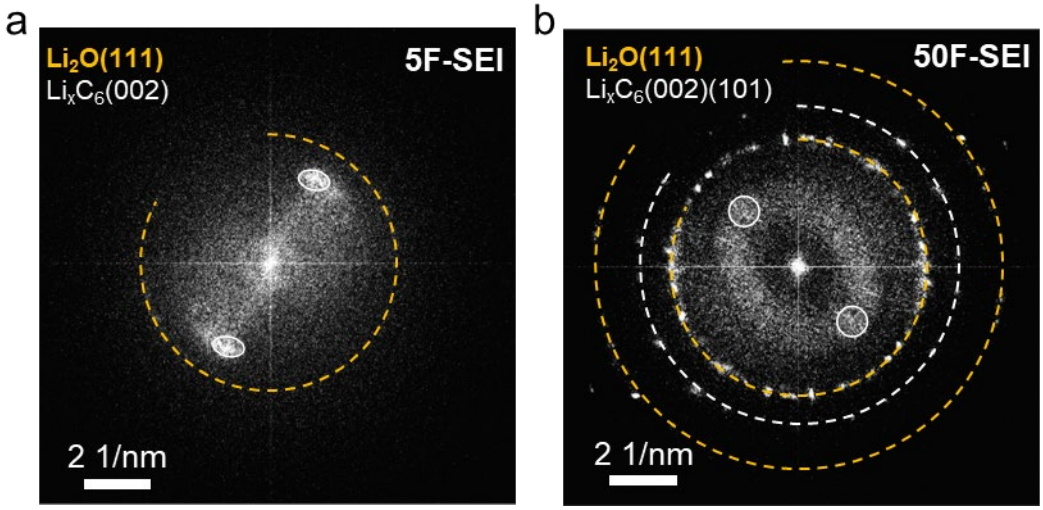

Fig. S11.

FFT analysis on structure and composition of SEI: (a) organic-rich SEI at 5 μA·cm^{-2}; (b) inorganic-rich SEI at 50 μA·cm^{-2} (denote as 50F-SEI).

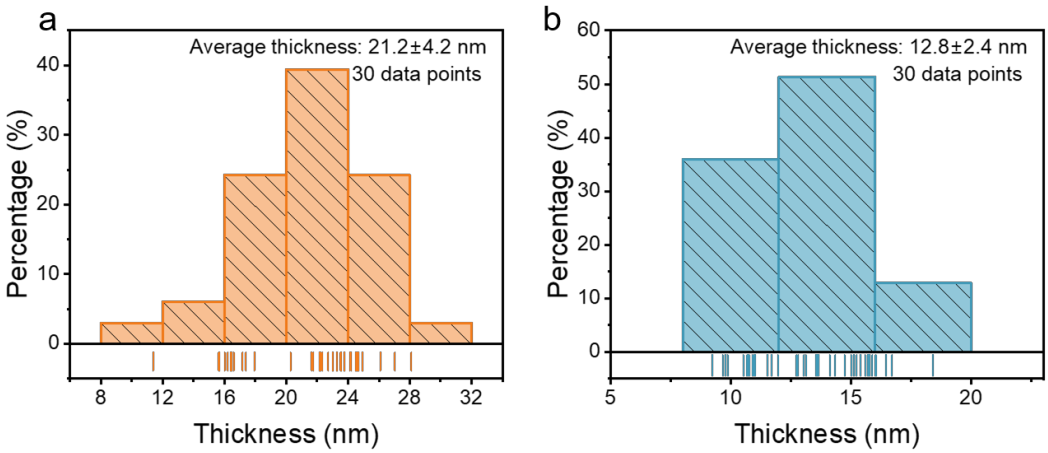

Fig. S12.
Thickness statistics of (a) 5F-SEI, (b) 50F-SEI

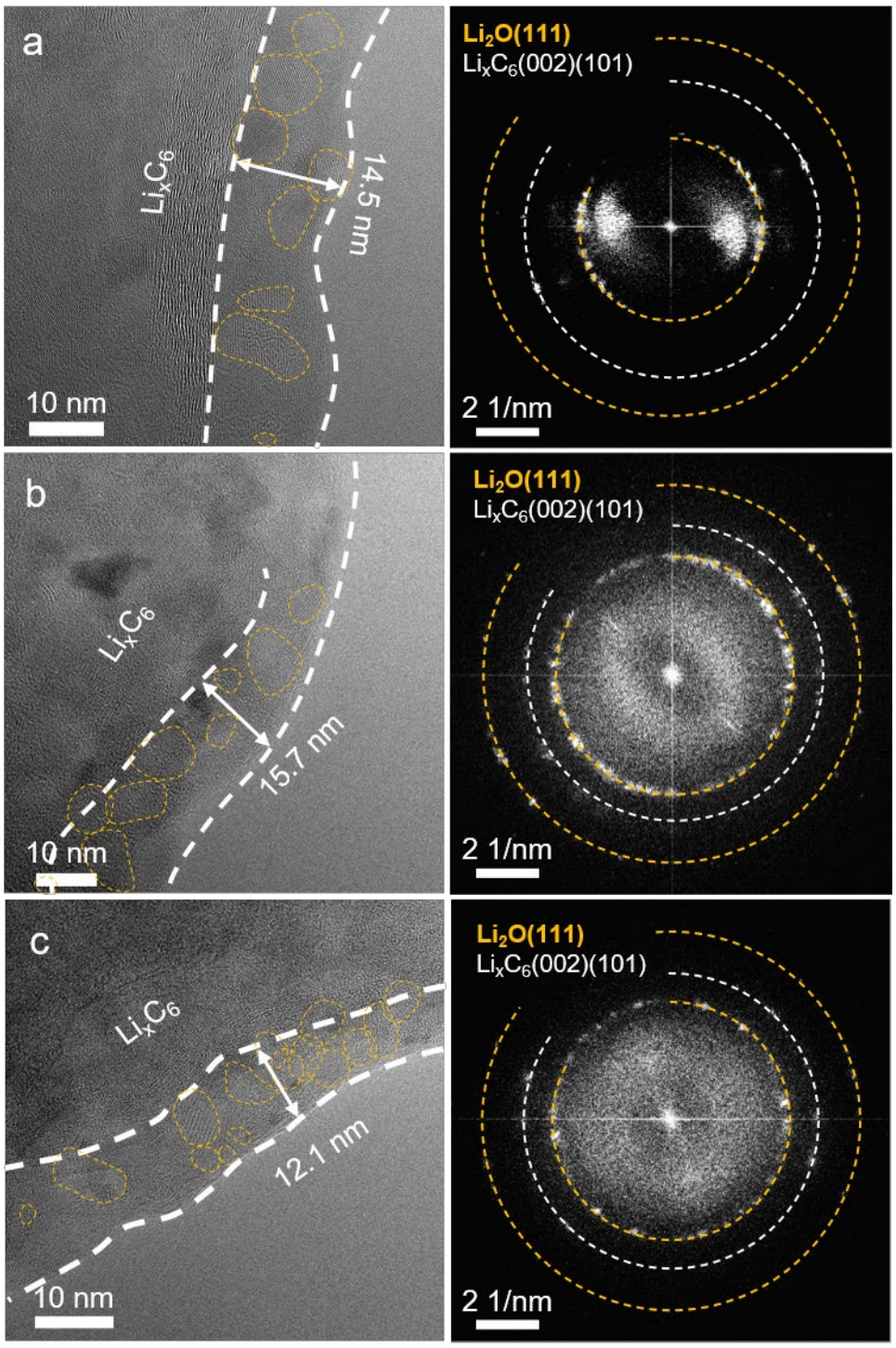

Fig. S13.

Consistent structure and composition of the inorganic-rich SEI (50F-SEI). Cryo-TEM images and corresponding FFT patterns from two independent graphite particles are shown in (a), (b) and (c), respectively.

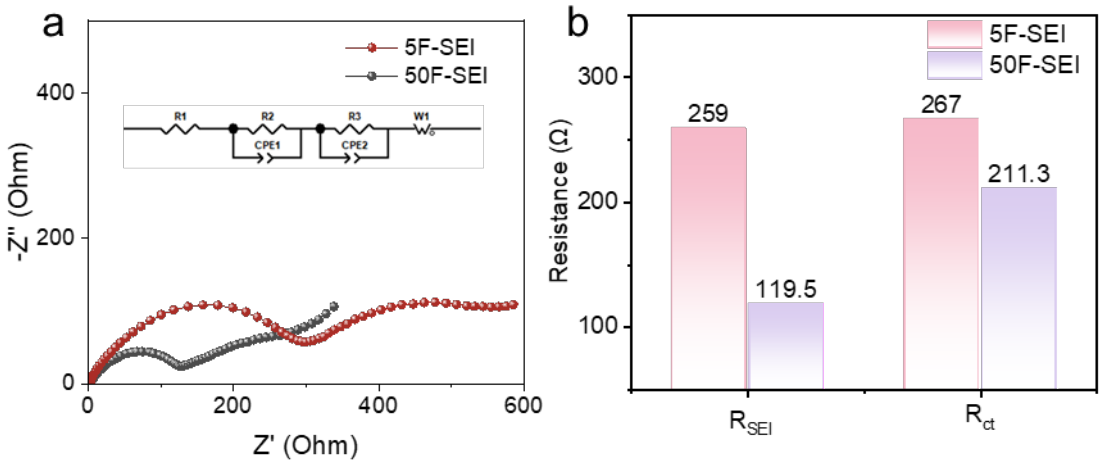

Fig. S14.

(a) Nyquist plots for 5F-SEI and 50F-SEI (inset: equivalent circuit model). (b) R_{ct} and R_{SEI} obtained by fitting the equivalent circuit in panel d.

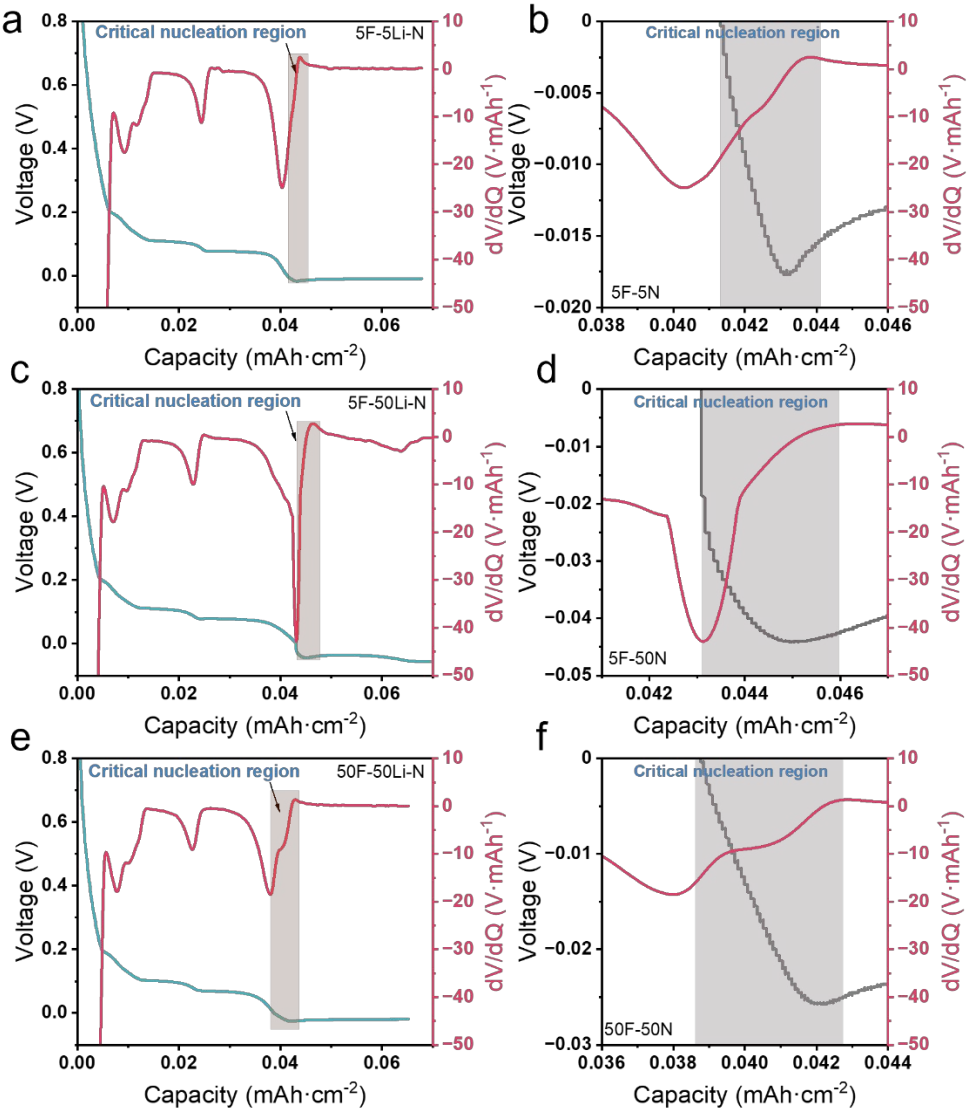

Fig. S15.

Electrochemical signatures of Li nucleation on pre-formed SEIs. (a, c, e) Voltage profiles (black) and differential capacity curves (dV/dQ, red) during Li plating on MGE electrodes with different SEI formation and nucleation current densities: (a) 5F-5Li-N (5 μA cm^{-2} during formation, 5 μA cm^{-2} during Li plating), (c) 5F-50Li-N (5 μA cm^{-2} during formation, 50 μA cm^{-2} during Li plating), (e) 50F-50Li-N (50 μA cm^{-2} during formation, 50 μA cm^{-2} during Li plating). (b, d, f) Magnified views of the nucleation onset region, highlighting the thermodynamic nucleation potential P1 (0 V *vs.* Li^+/Li) and kinetic endpoint P2 (dV/dQ = 0).

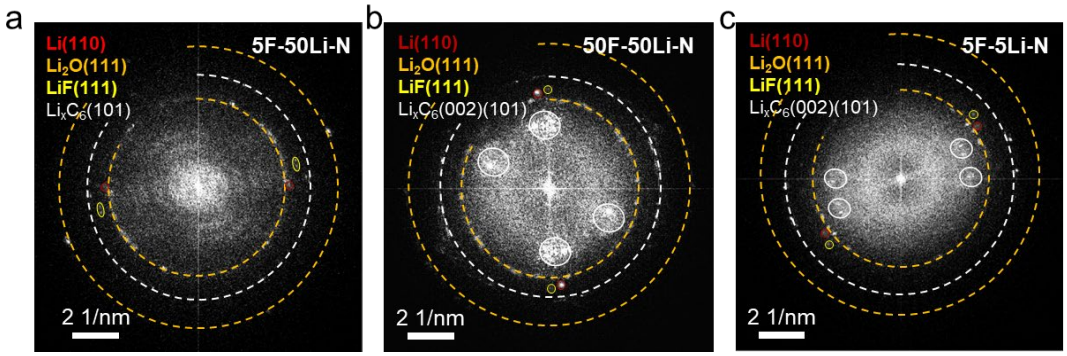

Fig. S16.

FFT analysis of SEI structure and composition. Representative FFT patterns obtained from cryo-TEM images of Li nucleation sites: (a) 5F-50Li-N; (b) 50F-50Li-N; (c) 5F-5Li-N.

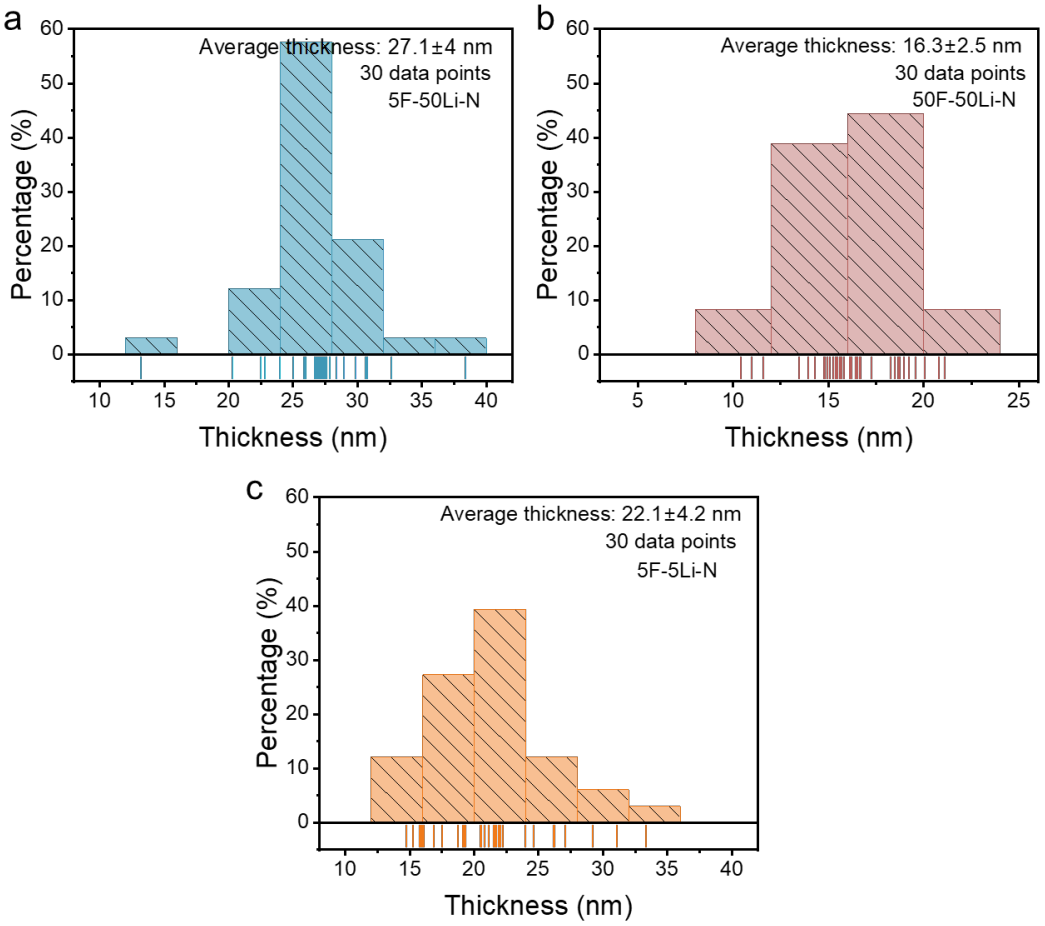

Fig. S17.
Thickness statistics of Li nucleation in the SEI: (a) 5F-50Li-N; (b) 50F-50Li-N; (c) 5F-5Li-N.

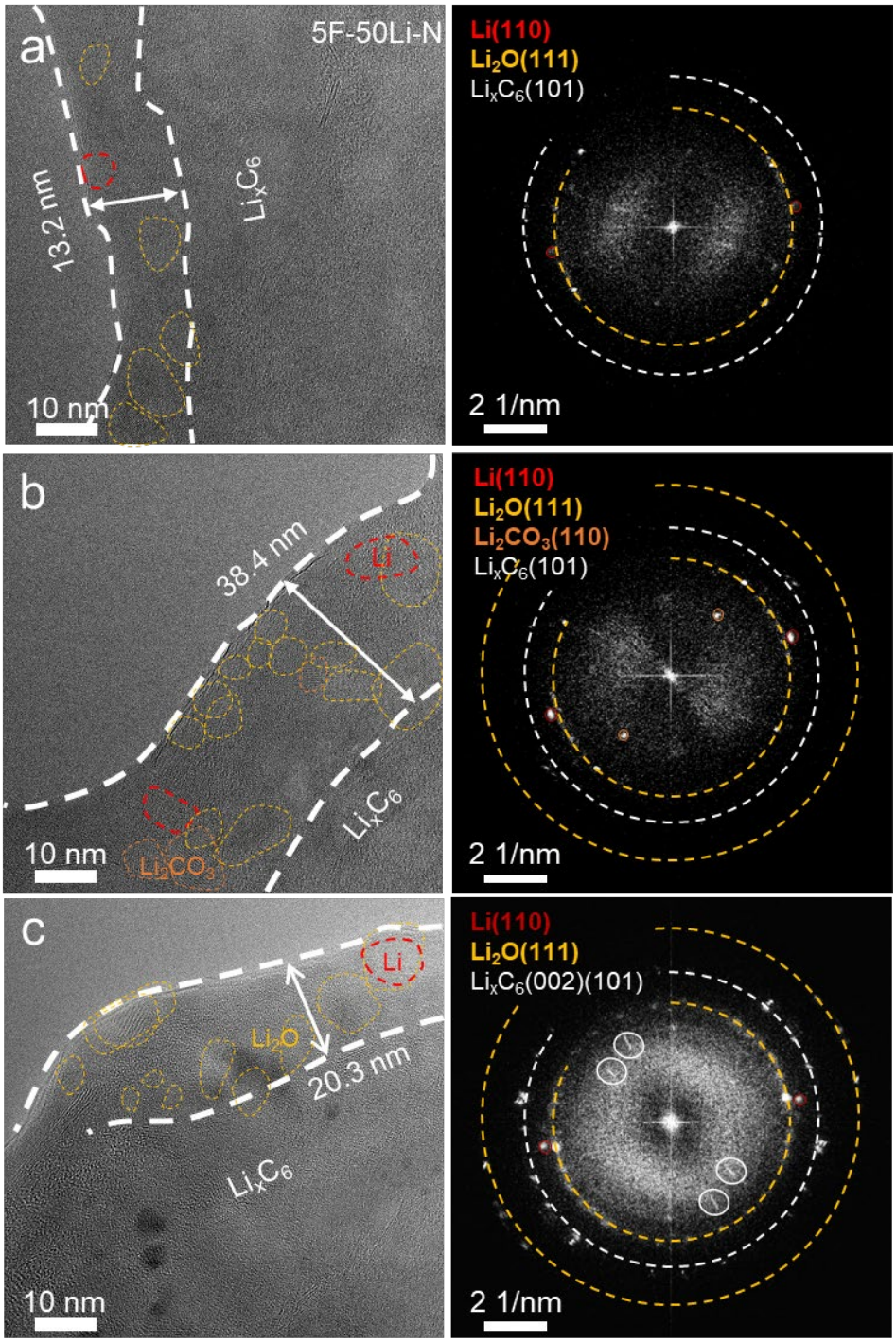

Fig. S18.

The structure and composition of Li nucleated within the 5F-SEI at 50 μA·cm^{-2}. Cryo-TEM images and corresponding FFT patterns from three independent graphite particles are shown in (a), (b) and (c), respectively.

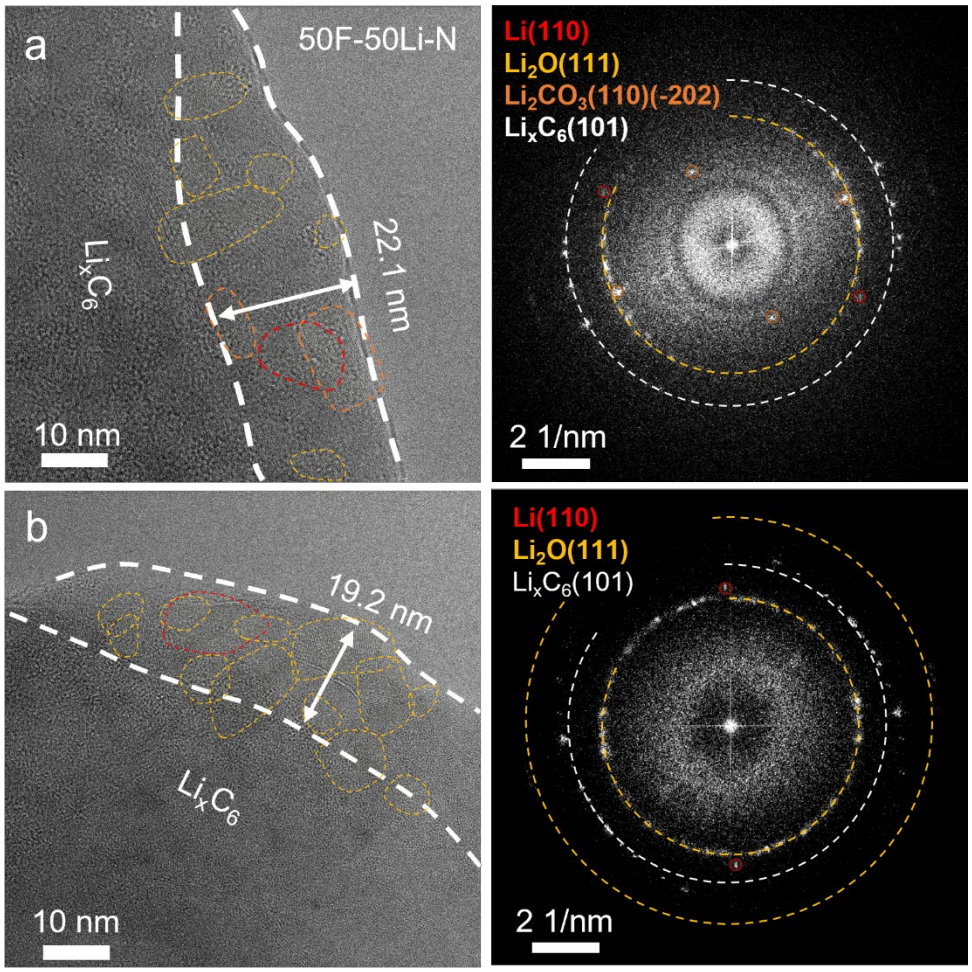

Fig. S19.

The structure and composition of Li nucleated within the 50F-SEI at 50 μA·cm^{-2}. Cryo-TEM images and corresponding FFT patterns from two independent graphite particles are shown in (a) and (b), respectively.

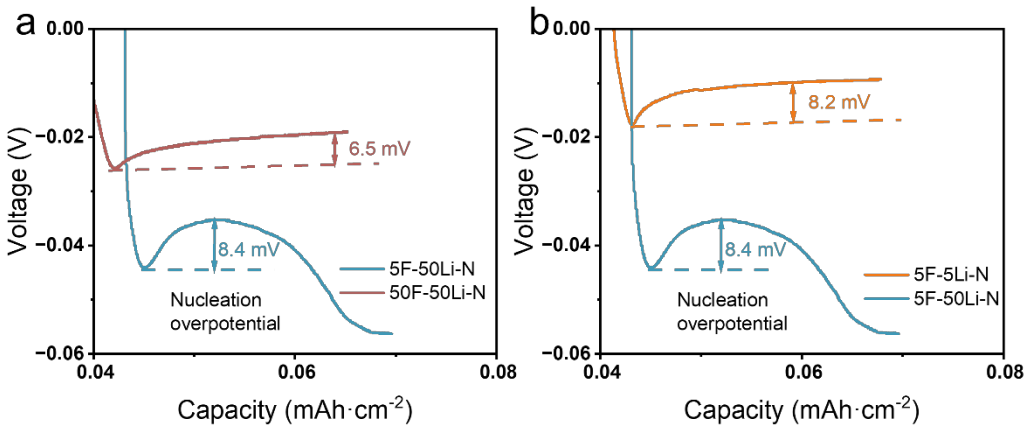

Fig. S20.
Comparison of nucleation overpotential (a) 5F-50Li-N and 50F-50Li-N; (b) 5F-5Li-N and 5F-50Li-N;

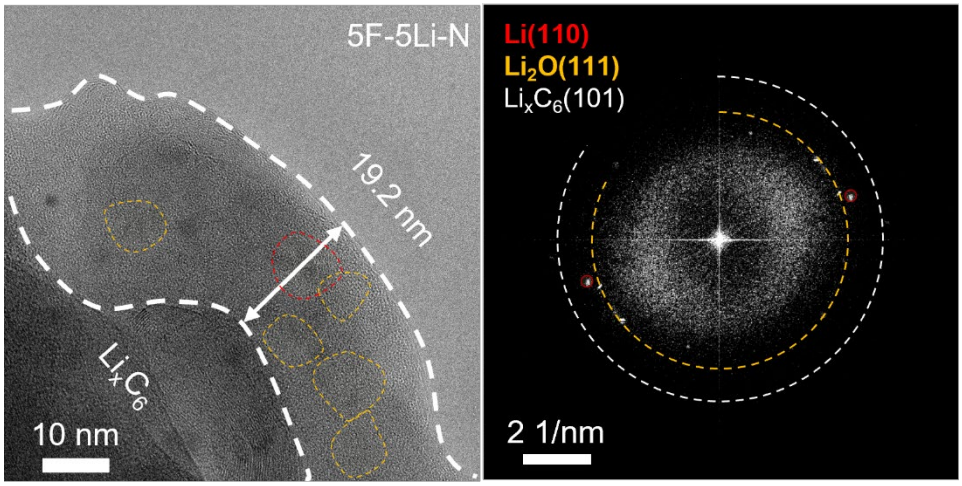

Fig. S21.
The structure and composition of Li nucleated within the 5F-SEI at 5 μA·cm^{-2}. Cryo-TEM images and corresponding FFT patterns from graphite particles.

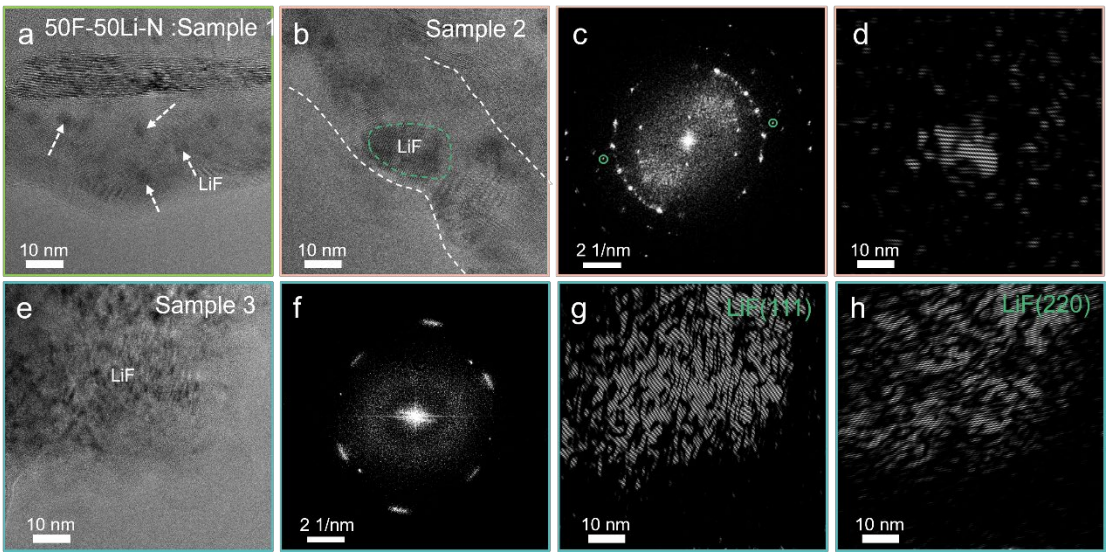

Fig. S22.

Cryo-TEM of LiF formation in 50F-50Li-N. (a-b, e) Heterogeneous LiF distribution: dispersed nanograins (arrows) and agglomerates (dashed lines). (c, f) FFT patterns confirming rock-salt structure. (d) Inverse FFT from (c) showing lattice fringes. (g-h) Inverse FFT reconstructions from (111) and (220) reflections. Direct evidence for cascading reduction reactions enriching inorganic phases (LiF).

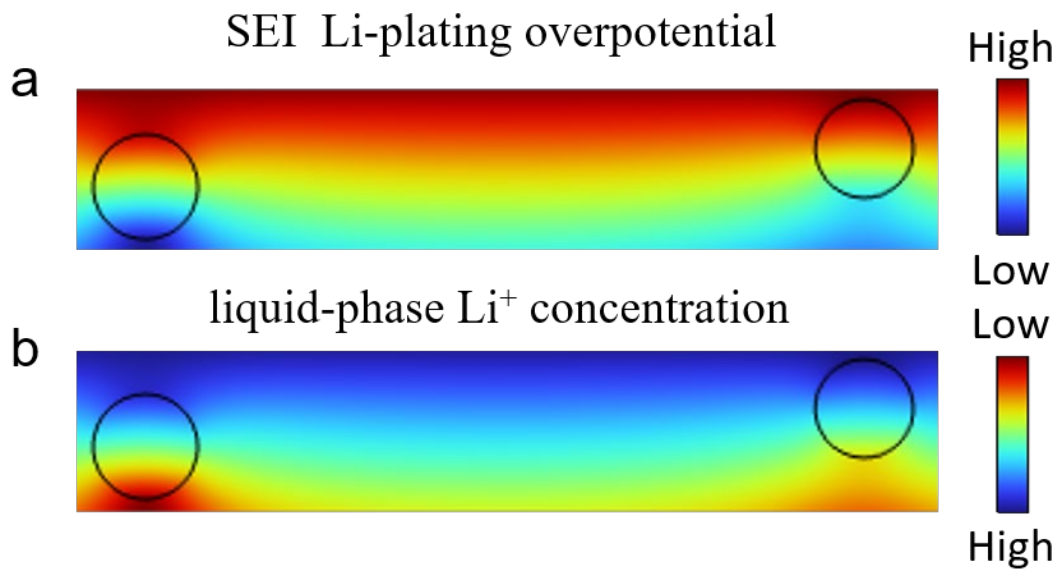

Fig. S23.
2D multi-physics simulations of organic-rich SEI chemistries. (a) Li-plating overpotential and (b) liquid-phase Li^+ concentration.

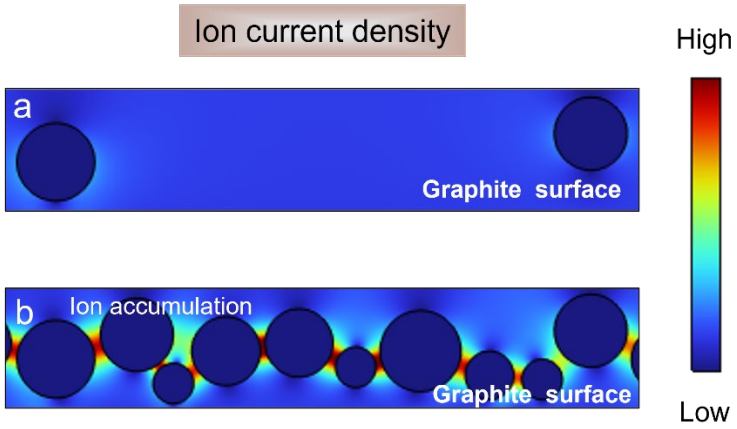

Fig. S24.
Simulated ionic current density distribution in organic-rich SEI (a) and inorganic-rich SEI (b).

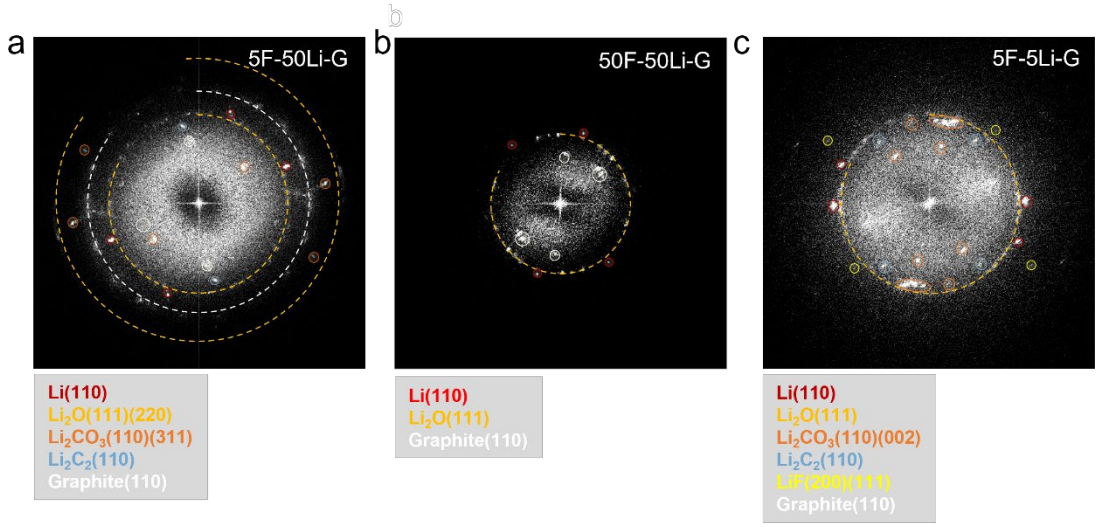

Fig. S25.
FFT analysis of SEI structure and composition. Representative FFT patterns obtained from cryo-TEM images of Li nucleation-growth sites: (a) 5F-50Li-N; (b) 50F-50Li-N; (c) 5F-5Li-N.

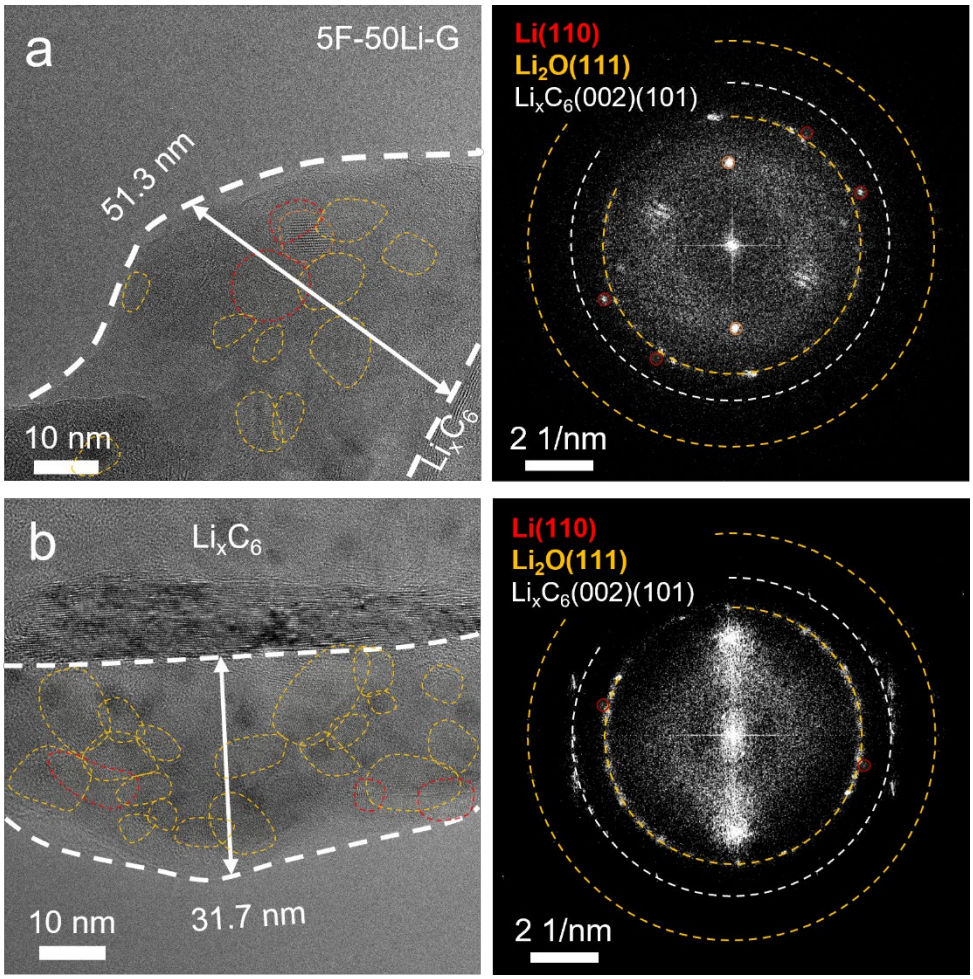

Fig. S26.

The structure and composition of Li growth within the 5F-SEI at 50 μA·cm^{-2}. Cryo-TEM images and corresponding FFT patterns from two independent graphite particles are shown in (a) and (b), respectively.

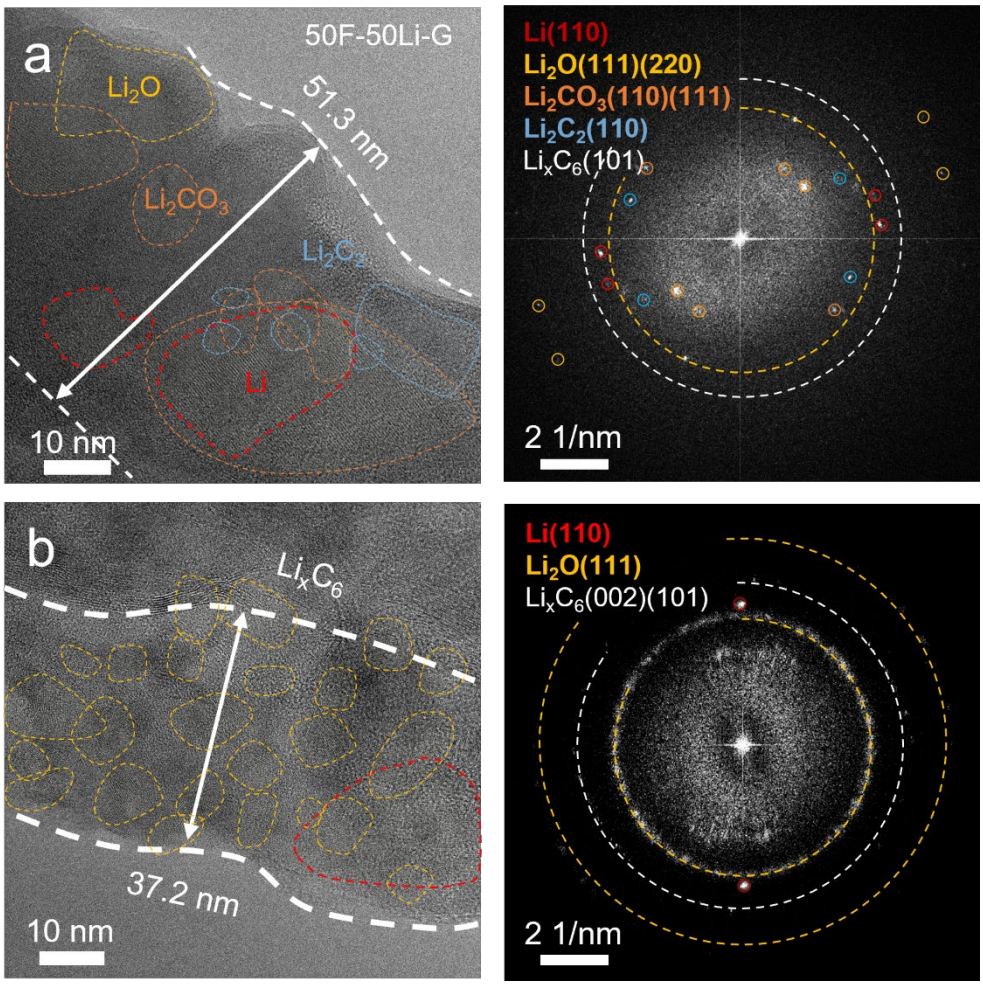

Fig. S27.

The structure and composition of Li growth within the 50F-SEI at 50 μA·cm^{-2}. Cryo-TEM images and corresponding FFT patterns from two independent graphite particles are shown in (a) and (b), respectively.

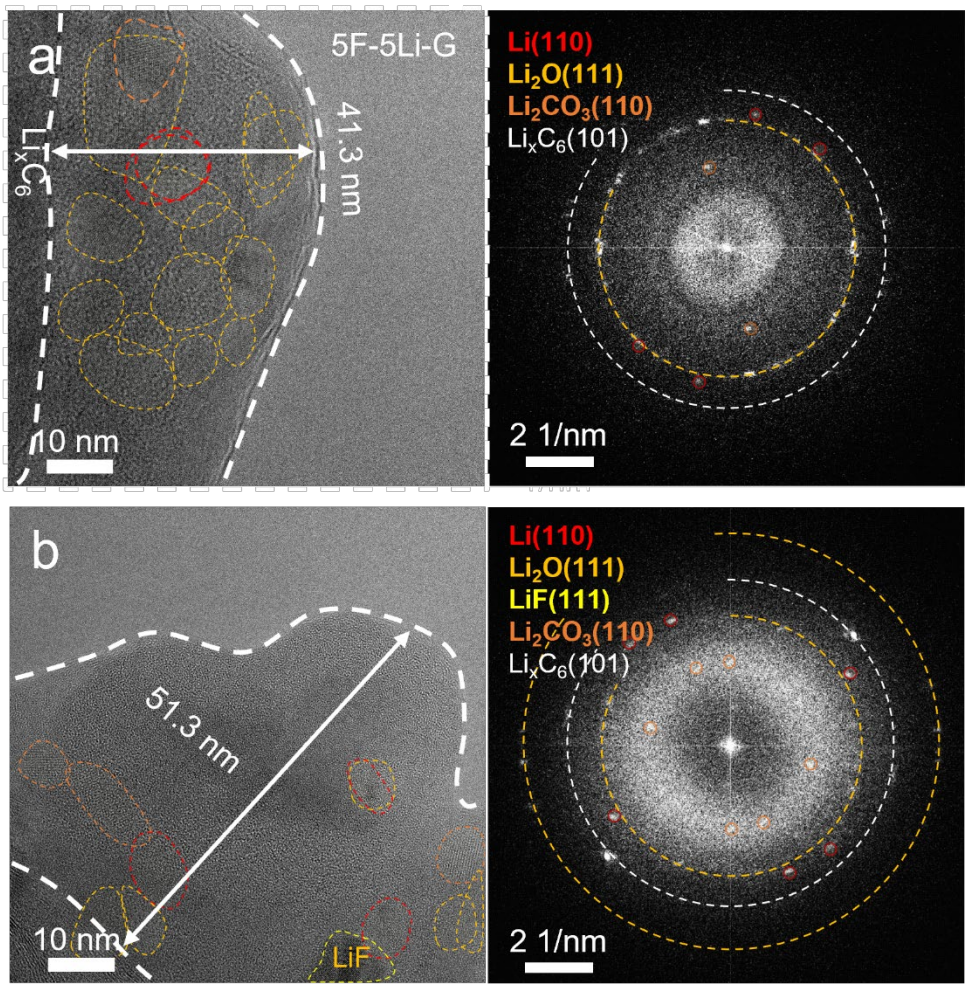

Fig. S28.

The structure and composition of Li growth within the 5F-SEI at 5 μA·cm^{-2}. Cryo-TEM images and corresponding FFT patterns from two independent graphite particles are shown in (a) and (b), respectively.

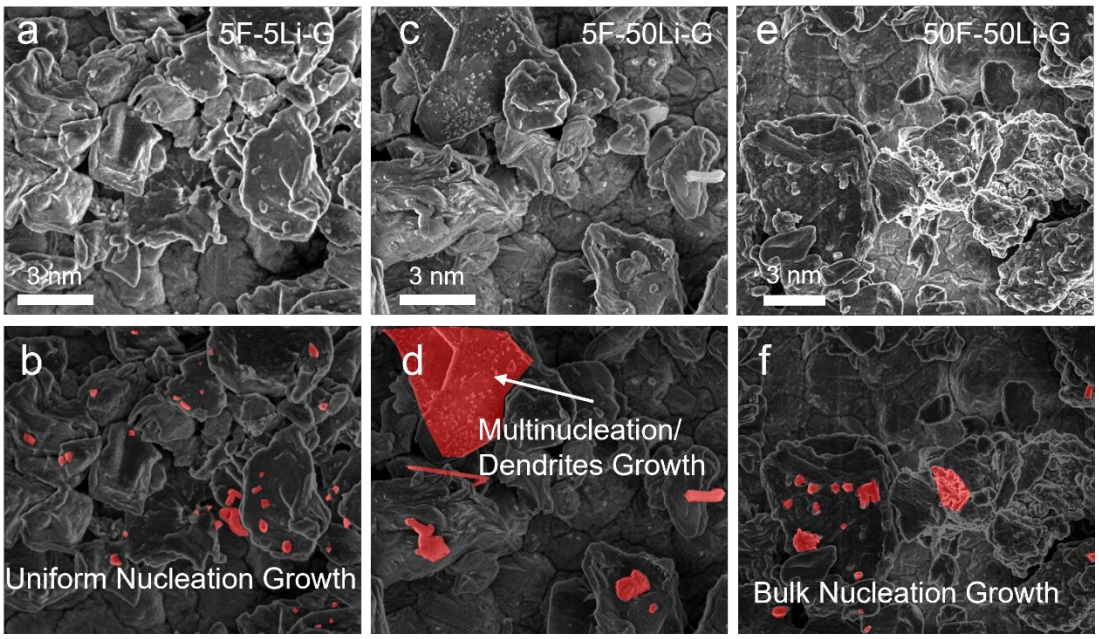

Fig. S29.

SEM imaging of Li nucleation to 0.02mAh cm^{-2} under three conditions: (a-b)5F-5Li-N, (c-d) 5F-50Li-N, (e-f) 50F-50Li-N.

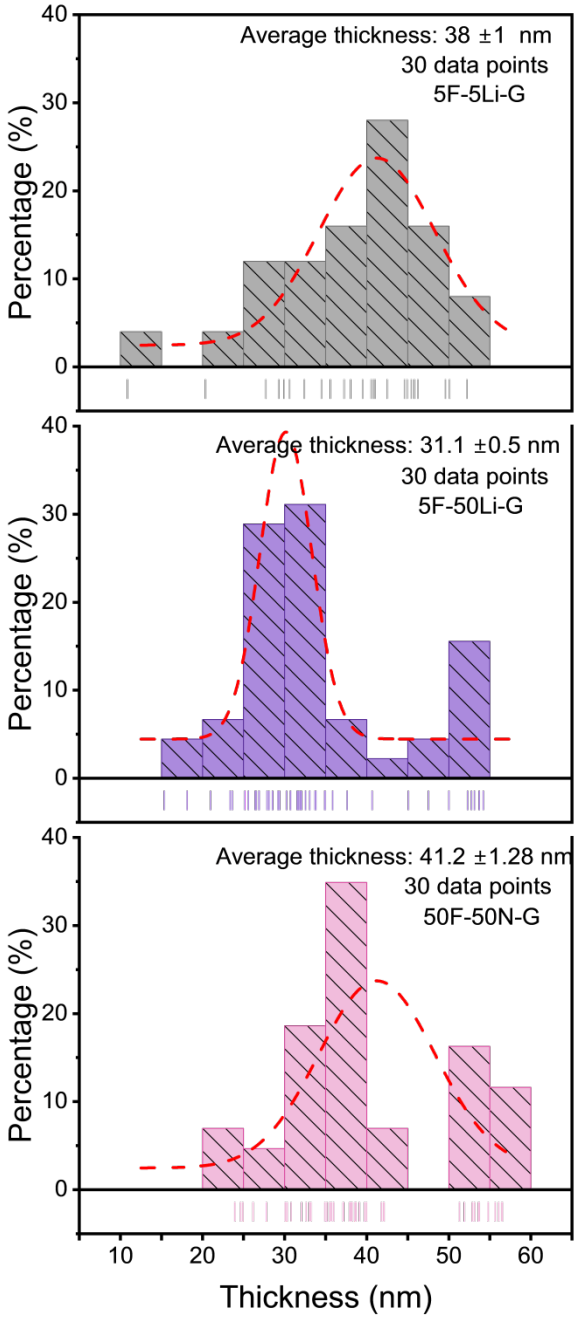

Fig. S30.
Thickness statistics of Li growth in the SEI under three conditions: 5F-50Li-G, 50F-50Li-G, 5F-5Li-G.

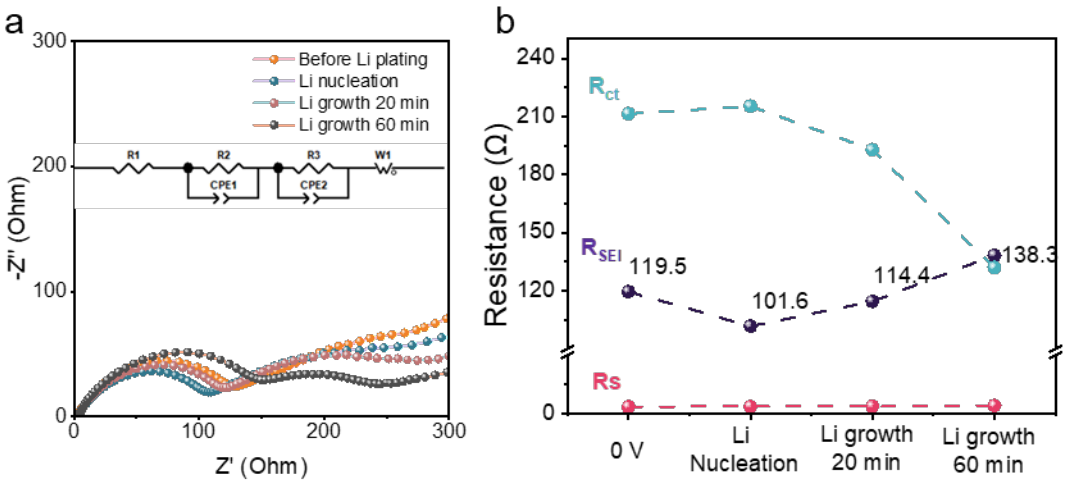

Fig. S31.

(a) Nyquist plots of electrochemical impedance spectra at different Li plating stages, with curves corresponding to the states before Li plating, Li nucleation, Li growth for 20 min, and Li growth for 60 min, respectively. (b) Evolution of solution resistance (R_s), charge transfer resistance (R_{ct}), and SEI resistance (R_{SEI}) obtained from fitting via the equivalent circuit.

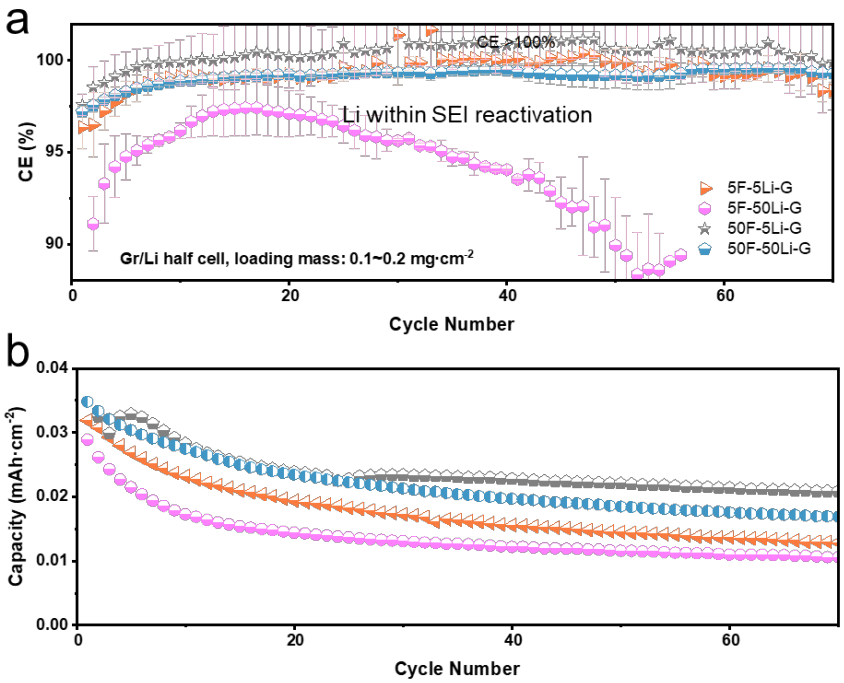

Fig. S32.

Monolayer graphite electrodes (areal loading: 0.1-0.2 mg cm^{-2}): (a) CE of Gr‖Li half-cells under four rate combinations defined as formation rate-Li nucleation rate 5F-5Li-G, 5F-50Li-G, 50F-5Li-G, and 50F-50Li-G; (b) Corresponding discharge-capacity retention.

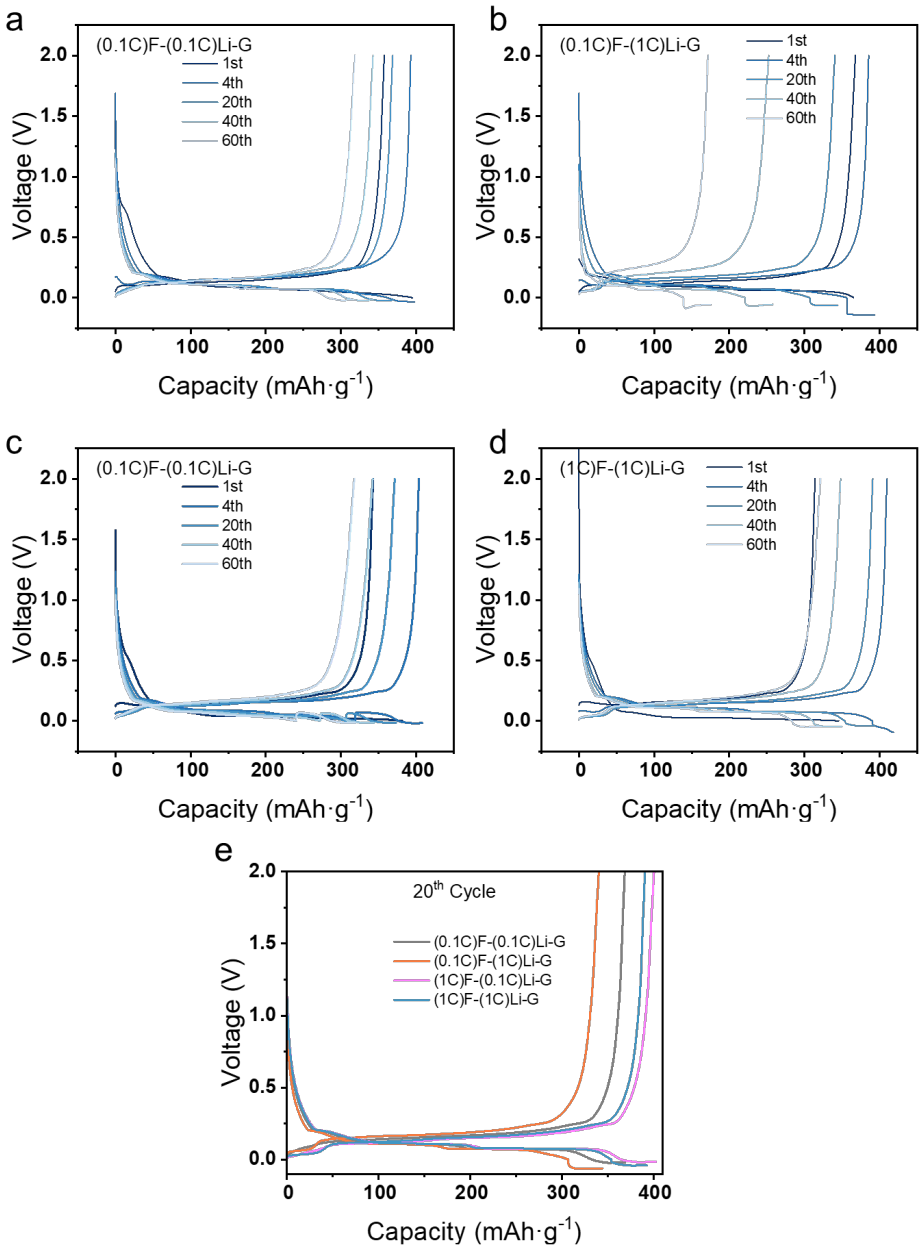

Fig. S33.
Electrochemical performance of various conditions in graphite|Li half-cells. The specific capacities were controlled to achieve 110% state of charge (SOC) (overlithiation). Li plating/stripping voltage profiles are shown for (a) ((0.1C)F-(0.1C)Li-G, (b) (0.1C)F-(1C)Li-G, (c) (1C)F-(0.1C)Li-G, and (d) (1C)F-(1C)Li-G)) at various cycles. (e) Comparison of the four conditions at the 20th cycle. (f) Enlarged view of (e).

References and Notes

1. E. Peled, The Electrochemical Behavior of Alkali and Alkaline Earth Metals in Nonaqueous Battery Systems—The Solid Electrolyte Interphase Model. *Journal of The Electrochemical Society* **126**, 2047–2051 (1979).
2. K. Tasaki, Solvent decompositions and physical properties of decomposition compounds in Li-ion battery electrolytes studied by DFT calculations and molecular dynamics simulations. *The Journal of Physical Chemistry B* **109**, 2920–2933 (2005).
3. S. Shi *et al.*, Direct Calculation of Li-Ion Transport in the Solid Electrolyte Interphase. *Journal of the American Chemical Society* **134**, 15476–15487 (2012).
4. M. Feng, J. Pan, Y. Qi, Impact of Electronic Properties of Grain Boundaries on the Solid Electrolyte Interphases (SEIs) in Li-ion Batteries. *The Journal of Physical Chemistry C* **125**, 15821–15829 (2021).
5. S. Perez-Beltran, D. Kuai, P. B. Balbuena, SEI Formation and Lithium-Ion Electrodeposition Dynamics in Lithium Metal Batteries via First-Principles Kinetic Monte Carlo Modeling. *ACS Energy Letters* **9**, 5268–5278 (2024).
6. Y. Xu *et al.*, Direct in situ measurements of electrical properties of solid–electrolyte interphase on lithium metal anodes. *Nature Energy* **8**, 1345–1354 (2023).
7. Y.-X. Yao *et al.*, Nucleation and Growth Mode of Solid Electrolyte Interphase in Li-Ion Batteries. *Journal of the American Chemical Society* **145**, 8001–8006 (2023).
8. F. T. Krauss, A. Duncker, B. Roling, Transport and Reaction of Electrons and Molecules in Solid Electrolyte Interphases formed at Different Electrode Potentials: A Combined Experimental and Modeling Approach. *ChemSusChem* **18**, (2025).
9. Y. An, T. Hu, Q. Pang, S. Xu, Observing Li Nucleation at the Li Metal–Solid Electrolyte Interface in All-Solid-State Batteries. *ACS Nano* **19**, 14262–14271 (2025).
10. K. Zhang *et al.*, Simulating solid electrolyte interphase formation spanning 108 time scales with an atomically informed phase-field model. *Energy & Environmental Science* **18**, 7541–7554 (2025).
11. H. Ge *et al.*, Investigating Lithium Plating in Lithium-Ion Batteries at Low Temperatures Using Electrochemical Model with NMR Assisted Parameterization. *Journal of The Electrochemical Society* **164**, A1050–A1060 (2017).
12. J. Newman, D. Bennion, C. h. W. Tobias, Mass Transfer in Concentrated Binary Electrolytes. *Physical Chemistry Chemical Physics* **69**, 608 (1965).
13. A. Zuo, R. Fang, Z. Wu, Z. Li, Diffusion-limited C-rate: a criterion of rate performance for lithium-ion batteries. *Journal of Energy Storage* **56**, 105920 (2022).
14. S. Park *et al.*, Liquid electrolyte chemistries for solid electrolyte interphase construction on silicon and lithium-metal anodes. *Chemical Science* **14**, 9996–10024 (2023).
15. R. Fang, H. Ge, Z. Wang, Z. Li, J. Zhang, A two-dimensional heterogeneous model of lithium-ion battery and application on designing electrode with non-uniform porosity. *Journal of The Electrochemical Society* **167**, 130513 (2020).
16. K. Zhang *et al.*, Simulating solid electrolyte interphase formation spanning 108 time scales with atomically informed phase-field model. *Energy & Environmental Science*, (2025).
17. B. Liu *et al.*, A quantitative figure of merit for battery SEI films and their use as functional solid-state electrolytes. *Proceedings of the National Academy of Sciences* **122**, e2425556122 (2025).

18. R. Fang, H. Ge, Z. Wang, Z. Li, J. Zhang, A Two-Dimensional Heterogeneous Model of Lithium-Ion Battery and Application on Designing Electrode with Non-Uniform Porosity. *Journal of The Electrochemical Society* **167**, (2020).
19. A. Zuo *et al.*, Can ultra-dense cathode agglomerates be treated as solid particles? Direct evidence from single high-nickel NCM particle microelectrode. *Energy Storage Materials* **79**, 104314 (2025).